Transient Plasma Photonic Crystals - A Route Towards Slow Ultra-intense Light?

LRAP 548

Robin Weissenbilder

A thesis presented for the degree of
Master of Science in Engineering,
Engineering Physics

LUND
UNIVERSITY

Division of Atomic Physics, LTH
Lund, Sweden
June 2018

Abstract

Periodic electron and ion density modulations in near critical density plasmas induced by counterpropagating femtosecond pulses of intensities on the order of 10^{15} to $10^{16}\,\mathrm{Wcm}^{-2}$ are described in a linear and stationary regime and investigated using particle-in-cell simulations in one and two dimensions. The periodic gratings produce transient plasma photonic crystals lasting up to several picoseconds with ultra-wide angle-selective band gaps on the order of $\Delta\omega/\omega_0 \approx 10-20\%$. The slow light effects and transmission of ultra-short pulses of intensities up to $10^{17}\,\mathrm{Wcm}^{-2}$ near the band gap are studied both as a function of frequency and angle of incidence, demonstrating group velocities which are consistently below those in a uniform plasma of the same average density. The velocities are found to approach zero near the gap at the cost of high reflection and dispersion. Furthermore, the effect of ion mass and driving pulse chirp on the transient structures are studied. Finally, the band gaps may be used to repeatedly reflect a short intense pulse in a waveguide-like fashion with effective propagation velocity as low as $\sim 10\%$ of the speed of light.

Acknowledgements

I would like to thank my supervisor Claes-Göran Wahlström for support, fruitful discussions and giving me the opportunity to work on this theoretical project in an otherwise largely experimental environment.

I would also like to thank my co-supervisor Henrik Ekerfelt, especially for guidance and discussions on particle-in-cell simulations.

This work was in part supported by the Swedish Research Council and the UK EPSRC funded Collaborative Computational Project in Plasma Physics - grant reference number EP/M022463/1.

Contents

Chapter 1

Introduction

Since the invention of the technique known as chirped pulse amplification (CPA) pulsed lasers have reached ever higher intensities with femtosecond pulses of intensities as high as $10^{22}\,\mathrm{Wcm}^{-2}$, far above the thresholds where traditional materials break down [1]. These ultra-high intensities have opened up the field of research known as relativistic optics [2], allowing among other things efficient acceleration of both ions and electrons, usually through the methods of target normal sheath acceleration (TNSA) and laser wakefield acceleration (LWFA) [3, 4]. These have the benefit of being much more compact than the massive conventional particle accelerators. Due to the large mass difference in ions and electrons the former is not directly accelerated by the ultra-high intensity laser but rather by electric fields established as the electrons are pulled away.

Recently, other methods of ion acceleration have been proposed such as chirped standing wave acceleration (CSWA) and relativistic slow light in near critical density plasmas (densities between those found in solids and gases) [5, 6]. In a very simplified picture, the principle of these two very different methods is the use of initially slow light to accelerate the ions. The speed of the light is then allowed to slowly accelerate to allow a continued acceleration of the ions in an efficient manner.

Slow light is defined by a group velocity which is much lower than the vacuum speed of light. Such slow light is often divided into two categories: material and structural slow light, which have been shown to be of very different character [7]. Material slow light is characterised by a group velocity of a light pulse which is inversely dependant on the change of refractive index with frequency, i.e. a rapid change in refractive index of a material, as a function of frequency, would drastically change the group velocity. Material slow light has even reached speeds as low as the speed of a bicycle by using ultra-cold gases [8]. Meanwhile, structural slow light is, as the name suggests, rather an effect of structural properties than material ones. A one dimensional example of this type of slow light would be a Fibre Bragg Grating (FBG), a type of photonic crystal, consisting of alternating sheets of materials with different refractive indices. As a simple picture this can be understood from the fact that at each interface light is both reflected and transmitted and as such on average it takes longer for the light to propagate [7].

Photonic crystals have been studied as far back as 1887 by Lord Rayleigh in the form of Bragg gratings. The research area got its name much later after papers published by Yablonovitch on full photonic band gaps in 1991 and has expanded immensely since [9]. Slow light in photonic crystals is used in for example delay lines in optical communication and slow light across wide frequency bands with low dispersion has been demonstrated in photonic crystal waveguides [10–12].

Photonic crystals and photonic band gaps are similar to the electron band structures of solid state physics. In the electron case one can describe the existence of the bands by starting from the discrete energy levels of a single atom where adding more atoms in periodic structures, each one giving more possible energy levels, slowly builds the allowed bands. In the case of photonic crystals the picture is reversed, by starting from a single slab of transparent material all photon energies are allowed to propagate with low reflection. Adding more layers of material gives rise to reflections at each interface, slowly building the band gaps through destructive interference. The band structures of photonic crystals has been exstensively studied in for example [13–15]. The effect of introducing layers of low density plasma has also gained attention, in this case they are often called plasma photonic crystals (PPCs) [16].

The ultra-high intensity pulses obtained with CPA would destroy all of these crystals, however periodic structures made completely out of density modulations in plasmas, produced from the standing wave formed by two counter-propagating pulses of intensities on the order of $10^{15}\,\mathrm{Wcm}^{-2}$, have been investigated theoretically and experimentally on the surface of solid density targets and in gas targets for optical manipulation such as analysis of high harmonics and pulse shaping [17–19]. Theoretical work has also been done on bulk density gratings in near critical density plasmas where angle dependent photonic band gaps have been observed [20–22].

This type of plasma grating, which exists on the picosecond time scale and hence is called transient plasma photonic crystal (TPPC), has much higher damage threshold than ordinary dielectric materials and could offer slow light propagation of ultra intense pulses and potentially open up for other schemes of ion acceleration if reliable sources of uniform near critical density targets can be produced, which is currently also of interest in order to investigate many other plasma phenomena [23].

The aim of this thesis is to theoretically investigate the slow light capabilities of TPPCs for ultra-intense pulses on the femtosecond scale and expand on previous result on the formation of the bulk density gratings by considering possible limiting experimental factors. This is achieved by plasma simulation using a particle-in-cell (PIC) code.

This thesis is divided into six chapters. Chapters 2-4 contain the necessary background and for completeness include rigorous derivations when possible. Broken down into constituents, chapter 2 begins by defining a plasma and introduces fundamental parameters in laser-plasma interactions followed by giving a detailed analytic description of the formation of plasma density gratings in the linear and stationary regimes as well as their dispersion relations. Chapter 3 briefly discusses the concept of slow light and its limitations. In chapter 4 a short description of the PIC code used in the simulations is described for the interested reader. Chapter 5 presents the results of simulations, making comparisons to previous work and discusses the slow light observed in the TPPCs. Chapter 6 contains conclusions of the work and gives an outlook with other possible ways of obtaining ultra intense slow light in plasma structures.

Chapter 2

Transient Plasma Photonic Crystals

2.1 Plasmas

In this chapter various essential concepts of plasmas and light-plasma interactions for laser pulses with intensities on the order of $10^{15}\,\mathrm{Wcm}^{-2}$ are described.

Plasma is considered the fourth state of matter along with solids, liquids and gases and is the the most abundant matter in the observable universe. The latter three are however much more common on earth, where plasmas only exist under special conditions, such as in lightning or in the laboratory.

A plasma is in principle an ionised gas, but to be considered a plasma it must display collective behaviour. This collective behaviour arises when enough particles have been ionised so that a single charged particle in the gas interacts with many other charged particles through the Coulomb force. This long range interaction is the main difference to the other three states of matter and is the reason for many unique properties and phenomena.

In the laboratory a plasma is produced either through kinetic effects, where an electric field is applied to accelerate electrons which through collisions further ionise the medium, or by photoionisation where photons excite electrons into continuum states. Since the effect of ionisation is gradual it is not possible to define a thermodynamic phase transition as between the other states of matter.

At equilibrium a plasma will be neutral in the absence of external effects as even a small deviation from neutrality imposes huge Coulomb forces which could only be balanced by thermal effects if the plasma had a temperature of several million Kelvin. Plasmas are still generally quite hot, in this thesis the unit used to describe electron and ion temperatures is $1\,\mathrm{eV} = 11605\,\mathrm{K}$.

To summarise, plasmas can be treated in a number of different cases and are divided into for example hot or cold, high or low degree of ionisation, high or low density and whether the plasma is magnetised or not. In this thesis the plasmas to be considered are cold, fully ionised and unmagnetised.

2.2 Plasma Frequency

In order to properly simulate laser plasma interaction, it is first necessary to consider the time and length scales at which the phenomena to be studied occur. The characteristic time scale of a plasma are the inverse of the plasma frequencies of the different particle species, of which the electron frequency is generally the most important.

An expression for the latter, denoted ω_{pe}, can be derived by considering a slab of cold electrons (thermal motion is neglected) and stationary ions with charge neutrality, i.e. $Zn_{\mathrm{i}} = n_{\mathrm{e}}$, where n_α ($\alpha = \mathrm{e,i}$) is the species density and Z is the ion charge. The slab has a width L along the x-axis and extends to infinity in y and z, see Figure 2.1. By shifting the electrons from their equilibrium by some small amount $\Delta x \ll L$, a positive charge region with charge density $\sigma = en_{\mathrm{e}}\Delta x$, where e is the elementary charge, forms on the left side and a region of opposite charge forms on the right side. The resulting electric field is $E_x = \sigma/\epsilon_0 = en_{\mathrm{e}}\Delta x/\epsilon_0$, where ϵ_0 is the vacuum permittivity.

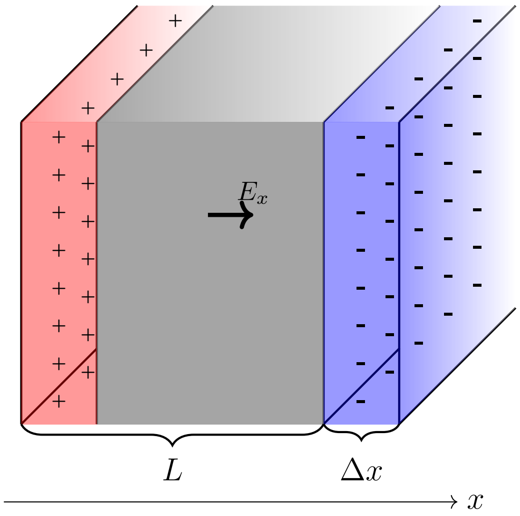

Figure 2.1: Neutral Plasma where electrons have shifted by Δx.

The force on one of the electrons is $F = -eE_x$, hence Newton's second law gives

$$\begin{aligned} m_{\mathrm{e}}\frac{\mathrm{d}^2\Delta x}{\mathrm{d}t^2} &= -eE_x = -\frac{e^2 n_{\mathrm{e}}}{\epsilon_0}\Delta x \quad \Leftrightarrow \\ \frac{\mathrm{d}^2\Delta x}{\mathrm{d}t^2} &+ \frac{e^2 n_{\mathrm{e}}}{\epsilon_0 m_{\mathrm{e}}}\Delta x = 0, \end{aligned} \tag{2.1}$$

where m_{e} is the mass of the electron. This is the standard harmonic oscillator where the natural frequency is identified as

$$\omega = \omega_{\mathrm{pe}} = \sqrt{\frac{e^2 n_{\mathrm{e}}}{\epsilon_0 m_{\mathrm{e}}}}. \tag{2.2}$$

The characteristic time scale is then $\tau_{\mathrm{pe}} \equiv 1/\omega_{\mathrm{pe}}$ and the inverse of particle mass shows why the electron plasma frequency is most important as this gives a natural limit on timescales. To reproduce plasma physics correctly in simulations it is generally desirable to have a time step which is smaller than τ_{pe}. Furthermore, only when the phenomena to be studied occur on timescales τ such that $\tau_{\mathrm{pe}} \ll \tau$ is the system considered to be a plasma [24, p. 5]. For a more rigorous derivation of the plasma frequency, see e.g. [25, p. 270].

For example, an electron density of $n_{\mathrm{e}} = 0.5 \cdot 10^{27}\,\mathrm{m}^{-3}$ gives a plasma frequency of $\omega_{\mathrm{pe}} \approx 1.3 \cdot 10^{15}\,\mathrm{s}^{-1}$ and a natural timescale of $\tau \approx 0.8\,\mathrm{fs}$.

2.3 Debye Length

Debye shielding is the screening of external electric fields from the interior of a plasma through the redistribution of charges in the plasma. The length at which this shielding takes place is the Debye length λ_{D}. In the following it is assumed the plasma is initially uniform and quasi-neutral plasma ($n_{\mathrm{e}} \simeq Zn_{\mathrm{i}} = n_0$) of electrons and ions where the species temperatures are assumed equal, $T_{\mathrm{i}} = T_{\mathrm{e}}$. The plasma is perturbed by a single positive charge Q at the origin. The goal is to find the resulting electrostatic potential, $\mathbf{E} = -\nabla\phi(\mathbf{r})$, close to the perturbing charge. Assuming the plasma is at thermal equilibrium, the species number densities take the form, given by the Maxwell-Boltzmann law [25, p. 274],

$$\begin{aligned} n_{\mathrm{e}} &= n_0 \exp\left[\frac{e\phi(\mathbf{r})}{k_{\mathrm{B}}T}\right], \\ n_{\mathrm{i}} &= n_0 \exp\left[-\frac{e\phi(\mathbf{r})}{k_{\mathrm{B}}T}\right], \end{aligned} \tag{2.3}$$

where n_0 is the number density far away from the charge perturbation and k_{B} is the Boltzmann constant.

Inserting equation (2.3) into Poisson's equation, the following expression is obtained

$$\begin{aligned} \nabla^2\phi(\mathbf{r}) &= \frac{e}{\epsilon_0}(n_{\mathrm{e}} - n_{\mathrm{i}}) - \frac{Q}{\epsilon_0}\delta(\mathbf{r}) = \\ \frac{en_0}{\epsilon_0}&\left(\exp\left[\frac{e\phi(\mathbf{r})}{k_{\mathrm{B}}T}\right] - \exp\left[-\frac{e\phi(\mathbf{r})}{k_{\mathrm{B}}T}\right]\right) - \frac{Q}{\epsilon_0}\delta(\mathbf{r}) \end{aligned} \tag{2.4}$$

where $\delta(\mathbf{r})$ is the Dirac delta function. Assuming the electrostatic energy is small compared to the thermal energy, $e\phi \ll k_{\mathrm{B}}T$, the two exponential functions can be expanded to $\exp\left[\pm\frac{e\phi(\mathbf{r})}{k_{\mathrm{B}}T}\right] \approx 1 \pm \frac{e\phi(\mathbf{r})}{k_{\mathrm{B}}T}$. The ones cancel and equation (2.4) can be rewritten as

$$\nabla^2\phi(\mathbf{r}) - \frac{2}{\lambda_{\mathrm{D}}^2}\phi(\mathbf{r}) = -\frac{Q}{\epsilon_0}\delta(\mathbf{r}), \tag{2.5}$$

where the Debye length has been identified as $\lambda_{\mathrm{D}} = \sqrt{\frac{\epsilon_0 k_{\mathrm{B}} T}{n_0 e^2}}$. This equation is most easily solved in Fourier space where it becomes

$$\left(k^2 + \frac{2}{\lambda_{\mathrm{D}}^2}\right)\phi(\mathbf{k}) = \frac{Q}{\epsilon_0} \quad \Leftrightarrow \quad \phi(\mathbf{k}) = \frac{Q}{\epsilon_0}\frac{1}{k^2 + \frac{2}{\lambda_{\mathrm{D}}^2}}. \tag{2.6}$$

The potential in real space follows after taking the inverse transform

$$\phi(\mathbf{r}) = \frac{1}{(2\pi)^3}\int \mathrm{d}^3k\, \frac{Q}{\epsilon_0}\frac{\mathrm{e}^{\mathrm{i}\mathbf{k}\cdot\mathbf{r}}}{k^2 + \frac{2}{\lambda_{\mathrm{D}}^2}} = \frac{Q}{4\pi\epsilon_0 r}\mathrm{e}^{-\frac{\sqrt{2}r}{\lambda_{\mathrm{D}}}}. \tag{2.7}$$

A similar expression can be obtained by assuming that the ions are stationary with a uniform number density n_0 equal to the unperturbed electron number density, in which case the factor $\sqrt{2}$ in equation (2.7) disappears [26, p. 14]. In any case, the potential shows that at lengths greater than the Debye length the electric field of the perturbing charge is screened, hence to be able to assume macroscopic charge neutrality it is necessary to consider phenomena which occur on length scales L such that $\lambda_{\mathrm{D}} \ll L$ holds [24, p. 5].

Continuing on the example given for the plasma frequency, for a number density $n_0 = 0.5 \cdot 10^{27}\,\mathrm{m}^{-3}$ and a temperature $T = 25\,\mathrm{eV}$ the Debye length is $\lambda_{\mathrm{D}} \approx 1.7\,\mathrm{nm}$.

2.4 Electromagnetic Waves in Plasmas

Plasmas can sustain a number of different types of wave phenomena depending on for example the existence and direction of magnetic fields in relation to the direction of the wave vector k. Indeed, one type has already been shown, namely the natural oscillation of electrons. This is however not a travelling wave and as such permits no propagation of energy/information. To study the properties of waves in physics it is common to find dispersion relations, which are equations relating the frequency to the wavenumber. From these it is then possible to find such things as the phase velocity, group velocity, dispersion, band gaps and more.

In this section the theory of electromagnetic wave propagation in plasmas will be considered by finding the dispersion relation subject to the following approximations (the conditions can be relaxed somewhat by not including condition iv [25, p. 402]):

i Homogeneous & infinitely extending plasma

ii Cold plasma ($\nabla p = 0$)

iii No external magnetic field ($\mathbf{B}_0 = \mathbf{0}$)

iv Collisionless plasma ($\nu \ll \omega$)

v Stationary ions ($\omega_{pi} \ll \omega$)

where ∇p is the pressure gradient, ν is the collision frequency, ω_{pi} and ω are the ion plasma frequency and electromagnetic wave frequency. For convenience the index e denoting electrons is dropped from all quantities as currently the ions are not of any concern.

Under these conditions and for small amplitude waves, the light-plasma interaction is described by the zeroth and first order moments of the distribution function[*], which are the electron number density $n(\mathbf{r}, t)$ and the average electron velocity $\mathbf{u}(\mathbf{r}, t)$, through the linearised force equation

$$m\frac{\mathrm{D}\mathbf{u}}{\mathrm{D}t} = q(\mathbf{E} + \mathbf{u} \times \mathbf{B}), \tag{2.8}$$

and Maxwell's equations

$$\nabla \cdot \mathbf{E} = \frac{\rho}{\epsilon_0}, \tag{2.9}$$

$$\nabla \cdot \mathbf{B} = 0, \tag{2.10}$$

$$\nabla \times \mathbf{E} = -\frac{\partial \mathbf{B}}{\partial t}, \tag{2.11}$$

$$\nabla \times \mathbf{B} = \mu_0 \left(\mathbf{J} + \epsilon_0 \frac{\partial \mathbf{E}}{\partial t} \right), \tag{2.12}$$

where $\frac{\mathrm{D}}{\mathrm{D}t} \equiv \frac{\partial}{\partial t} + \mathbf{u} \cdot \nabla$ is the total derivative[†]. The electron number density enters through the current density $\mathbf{J} = -en\mathbf{u}$ which depends only on the electrons because the ions were assumed stationary.

Assuming wave solutions of the form

$$\mathbf{E}(\mathbf{r}, t) = \mathbf{E}(\mathbf{r})\mathrm{e}^{-\mathrm{i}\omega t} \tag{2.13}$$

and neglecting second order terms such as $\mathbf{u} \cdot \nabla\mathbf{u}$ and $\mathbf{u} \times \mathbf{B}$, equation (2.8) reduces to (this is valid when $u \ll \omega/k$ [25, p. 403])

$$\frac{\partial \mathbf{u}}{\partial t} = \frac{q}{m}\mathbf{E}(\mathbf{r})\mathrm{e}^{-\mathrm{i}\omega t}. \tag{2.14}$$

Taking the time derivative of $\mathbf{J}$ and inserting into equation (2.14) yields

$$\frac{\partial \mathbf{J}}{\partial t} = -en\frac{\partial \mathbf{u}}{\partial t} = \frac{e^2 n}{m}\mathbf{E}(\mathbf{r})\mathrm{e}^{-\mathrm{i}\omega t} = \omega_{\mathrm{p}}^2 \epsilon_0 \mathbf{E}(\mathbf{r})\mathrm{e}^{-\mathrm{i}\omega t}, \tag{2.15}$$

where the electron plasma frequency ω_{p} in equation (2.2) has been used. After integration the current is found to be

$$\mathbf{J} = \frac{\mathrm{i}\omega_{\mathrm{p}}^2 \epsilon_0}{\omega}\mathbf{E}(\mathbf{r})\mathrm{e}^{-\mathrm{i}\omega t}. \tag{2.16}$$

---

[*] The n:th moment of a point quantity f is simply $r^n f$ where r is a distance, for example the first few moments of mass are: total mass, centre of mass and moment of inertia ($n = 0, 1, 2$). The distribution function describes the ensamble average distribution in $(\mathbf{r}, \mathbf{v})$-space (phase space).

[†] The total derivative is also known under many other names, e.g. material derivative and Lagrangian derivative. It is easily obtained by the multivariate chain rule.

With this expression for the current density, equation (2.12) becomes

$$\nabla \times \mathbf{B} = -\mathrm{i}\omega\mu_0\epsilon_0\epsilon(\omega)\mathbf{E}(\mathbf{r})\mathrm{e}^{-\mathrm{i}\omega t}, \tag{2.17}$$

where the dielectric function in the plasma has been introduced as $\epsilon(\omega) = 1-\frac{\omega_\mathrm{p}^2}{\omega^2}$. Taking the curl of equation (2.11) and (2.12), using the identity $\nabla \times (\nabla \times \mathbf{A}) = \nabla(\nabla \cdot \mathbf{A}) - \nabla^2\mathbf{A}$ and substituting gives the wave equations

$$-\nabla(\nabla \cdot \mathbf{E}) + \nabla^2\mathbf{E} + \frac{\omega^2}{c^2}\epsilon(\omega)\mathbf{E} = 0, \tag{2.18}$$

$$\nabla^2\mathbf{B} + \frac{\omega^2}{c^2}\epsilon(\omega)\mathbf{B} = 0. \tag{2.19}$$

Assuming transverse plane waves, i.e. the spatial part of of the field is of the form $\mathbf{E}(\mathbf{r}) = \mathbf{E_0}\mathrm{e}^{\mathrm{i}\mathbf{k}\cdot\mathbf{r}}$, with $\mathbf{k} \perp \mathbf{E_0}$, and carrying out the derivatives gives the dispersion relation in a homogeneous plasma

$$\omega^2 = c^2k^2 + \omega_\mathrm{p}^2. \tag{2.20}$$

It should be noted that when $\omega < \omega_\mathrm{p}$ the wavenumber $k = c^{-1}\sqrt{\omega^2 - \omega_\mathrm{p}^2}$ is purely imaginary. Inserting this wavenumber into the spatial part of the plane wave gives $\mathbf{E}(\mathbf{r}) = \mathrm{e}^{-\mathrm{Im}(\mathbf{k})\cdot\mathbf{r}}$ which is an exponentially decaying wave, hence frequencies below the cutoff frequency ω_p will not propagate. Recall that the plasma frequency depends on the electron number density, it is then possible to define a cutoff density from the condition $\omega = \omega_\mathrm{p}$ called the critical density, given by

$$n_\mathrm{c} = \frac{\epsilon_0 m_\mathrm{e}}{e^2}\omega^2. \tag{2.21}$$

Plasmas of densities below n_c are often called underdense whereas plasmas of densities exceeding n_c are called overdense. With this definition it is possible to rewrite the wavenumber as

$$k = k_0\sqrt{1 - n/n_\mathrm{c}}, \tag{2.22}$$

where $k_0 = \omega/c$ is the vacuum wavenumber.

Figure 2.2 shows the dispersion relation and cutoff frequency in comparison to the free space dispersion relation. It is seen that the plasma light wave asymptotically approaches the free space light wave in the high frequency limit or equivalently in the low electron density limit.

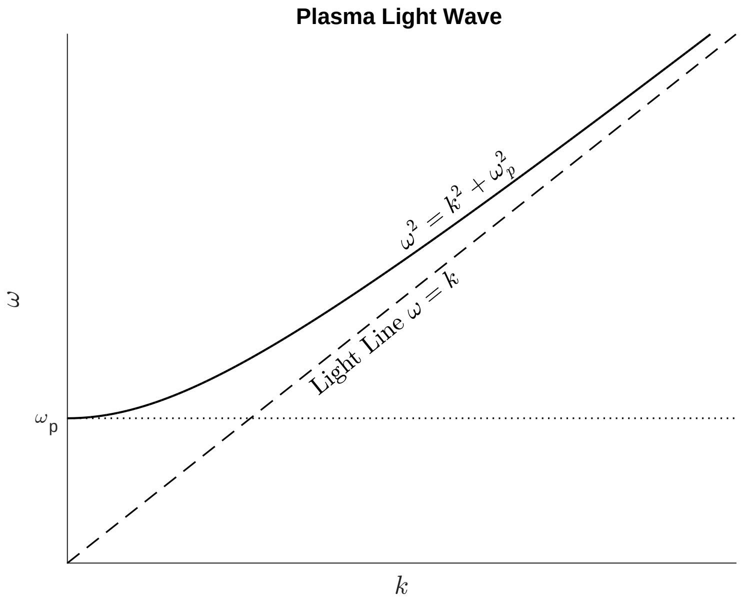

Figure 2.2: Dispersion relation (the speed of light has been set to $c = 1$) of a propagating plane wave sustained by a homogeneous plasma (solid line), dispersion relation of plane wave in vacuum (dashed line) and cutoff frequency ω_p (dotted line).

As a final note, if one assumes longitudinal waves ($\mathbf{k} \parallel \mathbf{E_0}$) in equation (2.18), the resulting dispersion relation turns out to be just $\omega_\mathrm{p}^2 = \omega^2$, which is to say longitudinal waves can be sustained for the conditions specified at the start of this section, but only as oscillations at the frequency exactly matching the natural oscillation frequency of electrons. In chapter 3 the phase and group velocities of these plasma waves and oscillations are discussed.

2.5 Ponderomotive Force

The ponderomotive force, which is a net force on charged particles subject to the oscillations of a light wave, has to be introduced before discussing how plasma density gratings can be formed through laser-plasma interactions. The field strengths used in the simulations in this thesis are non-relativistic to weakly relativistic ($I < 10^{18}\,\mathrm{Wcm}^{-2}$), hence a classical description of the ponderomotive force will suffice. Following the derivation of [27, p. 256-258], neglecting zero order field terms $\mathbf{B}_0$, $\mathbf{E}_0$, assuming a wave of the form

$$\mathbf{E} = \mathbf{E}(\mathbf{r}) \cos \omega t \tag{2.23}$$

and considering the motion of a single electron in this field, described by

$$m\frac{\mathrm{d}\mathbf{v}}{\mathrm{d}t} = -e\left(\mathbf{E} + \mathbf{v} \times \mathbf{B}\right). \tag{2.24}$$

As in the previous section, $\mathbf{v} \times \mathbf{B} = \mathbf{v}_1 \times \mathbf{B}_1 + \mathcal{O}(\mathbf{r}_3)$ is now second order and neglected to begin with. Inserting the field into the equation of motion evaluated at the initial position of the electron, $\mathbf{r}_0$, gives by integrating twice

$$m\frac{\mathrm{d}\mathbf{v}}{\mathrm{d}t} = -\mathbf{E}(\mathbf{r}_0)\cos\omega t \Rightarrow \tag{2.25}$$

$$\mathbf{v}_1 = -\frac{e}{m\omega}\mathbf{E}(\mathbf{r}_0)\sin\omega t = \frac{\mathrm{d}\mathbf{r}_1}{\mathrm{d}t} \Rightarrow \tag{2.26}$$

$$\Delta\mathbf{r}_1 = \frac{e}{m\omega^2}\mathbf{E}(\mathbf{r}_0)\cos\omega t, \tag{2.27}$$

where averaging over one period in the last expression one finds $\langle\Delta\mathbf{r}_1\rangle = 0$. Thus to first order the electron returns to its initial position and equation (2.27) describes the quiver motion in an electric field.

Proceeding to second order by Taylor expansion of the electric field around $\mathbf{r}_0$ results in

$$\mathbf{E} = \mathbf{E}\big|_{r=r_0} + (\Delta\mathbf{r}_1 \cdot \nabla)\mathbf{E}\big|_{r=r_0} + ..., \tag{2.28}$$

which should be combined with the previously neglected second order term $\mathbf{v}_1 \times \mathbf{B}_1$ to arrive at the equation of motion to second order. To do this $\mathbf{B}_1$ is first found using the Maxwell-Faraday equation

$$\nabla \times \mathbf{E} = -\frac{\mathrm{d}\mathbf{B}}{\mathrm{d}t} \Rightarrow \tag{2.29}$$

$$\mathbf{B}_1 = -\frac{1}{\omega}\nabla \times \mathbf{E}(\mathbf{r})\big|_{r=r_0}\sin\omega t. \tag{2.30}$$

The second order term of equation (2.24) is then

$$m\frac{\mathrm{d}\mathbf{v}_2}{\mathrm{d}t} = -e\left[(\Delta\mathbf{r}_1 \cdot \nabla)\mathbf{E} + \mathbf{v}_1 \times \mathbf{B}_1\right], \tag{2.31}$$

which after insertion of equations (2.26), (2.27) and (2.30) and averaging over one period and simplifying becomes

$$\left\langle\frac{\mathrm{d}\mathbf{v}_2}{\mathrm{d}t}\right\rangle = -\frac{e^2}{4m\omega^2}\nabla E^2(\mathbf{r}) \equiv \mathbf{f}_\mathrm{P}. \tag{2.32}$$

This is the ponderomotive force on a single particle, which by multiplication of a density n_0 becomes the force on a volume of particles

$$\mathbf{F}_\mathrm{P} = -\frac{\epsilon_0\omega_\mathrm{p}^2}{2\omega^2}\nabla\langle E^2\rangle, \tag{2.33}$$

where the constants have been expressed in the electron plasma frequency and $E^2(\mathbf{r}) = 2\langle E^2\rangle$ has been used. The ponderomotive force is interesting because it is independent of the sign of charge of the particle being affected, so that both electrons and ions will be pushed in the same direction. Furthermore it scales with the mass as $\mathbf{F}_{\mathrm{Pe}} = \frac{m_{\mathrm{e}}}{m_{\mathrm{i}}}\mathbf{F}_{\mathrm{Pi}}$ which will be used in the next section to neglect the force on protons. Finally, it can be seen that the particles will be pushed out of strong fields, into the troughs of the potential, independently of the polarisation of the field. In the general case including relativistic fields or particles the theory is usually much more complicated [28].

2.6 Laser Induced Plasma Density Gratings

In this section the interaction between two counterpropagating laser pulses forming a standing wave in an initially homogeneous underdense plasma is considered. A detailed derivation of the electron and ion motions due to the ponderomotive force is given in the linear regime, which for high intensity pulses is valid only for very short times. It does however provide some insight into the formation of the density variations as a result of the standing wave. To complement this picture a stationary solution of the density grating is also given, which is then used to estimate the maximum density and contrast* of the density grating. The derivations confirm previous expressions given in [20, 22].

The basic idea is this: The waves form a standing wave which through the ponderomotive force acts to push electrons into low intensity troughs forming density peaks. The moving electrons makes the plasma locally non-neutral which generates electrostatic fields. The ions are in turn accelerated by this field to restore neutrality. If the driving pulses are long, the standing wave will be present long enough to build a large density variation. As a consequence of this long-lasting standing wave, the ions will gain a large momentum so that they can reach the electron density peaks even after the driving pulses have propagated through the plasma. As a result of this large momentum the ions subsequently overshoot so that the density grating slowly dissipates.

2.6.1 Linear Solution

Plane waves are assumed counterpropagating along the $x-$axis which reduces the problem to one dimension, these waves are described by the vector potentials

$$\mathbf{a}_{1,2} = a_{1,2}\cos(k_{1,2}x - \omega_0 t)\mathbf{e}_y \tag{2.34}$$

where $k_2 = -k_1 = k_0\sqrt{1 - n_0/n_{\mathrm{c}}}$ is the wave vector in plasma as derived in section 2.4 and a is the vector potential normalised to mc^2/e. For convenience a is often related to the laser intensity I through

$$a = \lambda[\,\mu\mathrm{m}]\sqrt{7.3 \cdot 10^{-19} I[\,\mathrm{Wcm}^{-2}]}, \tag{2.35}$$

where λ is the laser wavelength.

---

*The contrast is defined as the ratio between the maximum and minimum density found in the structure.

The equations describing the laser-plasma interaction are [22]

$$\frac{\partial p_{\mathrm{e},x}}{\partial t} = c\frac{\partial(\phi - \bar{\gamma})}{\partial x}, \tag{2.36}$$

$$\frac{\partial n_{\mathrm{e}}}{\partial t} + c\frac{\partial(n_{\mathrm{e}} v_{\mathrm{e},x})}{\partial x} = 0, \tag{2.37}$$

$$\frac{\partial p_{\mathrm{i},x}}{\partial t} = -c\frac{m}{M}\frac{\partial \phi}{\partial x}, \tag{2.38}$$

$$\frac{\partial n_{\mathrm{i}}}{\partial t} + c\frac{\partial(n_{\mathrm{i}} v_{\mathrm{i},x})}{\partial x} = 0, \tag{2.39}$$

$$\frac{\partial^2 \phi}{\partial x^2} = \frac{\omega_{\mathrm{p}}^2}{c^2}(n_{\mathrm{e}} - Z n_{\mathrm{i}}), \tag{2.40}$$

where equations (2.36) and (2.38) are the simplified cold plasma fluid equations of motion for electrons and ions respectively (see appendix A for a derivation), equations (2.37) and (2.39) are the continuity equations for electrons and ions (implying conservation of mass) and equation (2.40) is Poisson's equation.

In these equations $p_{\mathrm{e},x}$ and $p_{\mathrm{i},x}$ are the electron and ion momentum x-components normalised to mc and Mc where m and M are the rest masses of electrons and ions, ϕ is the scalar potential normalised to mc^2/e, n_{e} and n_{i} are the electron and ion number densities normalised to the unperturbed density n_0, $v_{\mathrm{e},x}$ and $v_{\mathrm{i},x}$ are the electron and ion x-component velocities normalised to the speed of light c and $\bar{\gamma}$ is the relativistic factor time averaged over a laser cycle.

Here $\bar{\gamma}$ is to be interpreted as the ponderomotive potential. As mentioned before, the ponderomotive force is neglected from the ion equation of moment because of the way it scales with mass.

For plane waves it can be shown to be given by $\bar{\gamma} = \sqrt{1 + \langle \mathbf{a} \cdot \mathbf{a} \rangle}$ where $\langle \cdot \rangle$ denotes the time average over one laser cycle [29]. With the vector potentials in equation (2.34) the time averaged term for the standing wave is

$$\langle \mathbf{a} \cdot \mathbf{a} \rangle = a^2/2 = \frac{1}{2}\left[a_1^2 + a_2^2 + 2a_1 a_2 \cos(2k_1 x)\right] \tag{2.41}$$

Non-relativistic intensities and typical laser wavelengths imply $a \ll 1$. This allows $\bar{\gamma}$ to be expanded as $\bar{\gamma} \approx 1 + a^2/4$. With this approximation the ponderomotive force takes the form

$$F_P = -\frac{\partial \bar{\gamma}}{\partial x} = k_1 a_1 a_2 \sin(2k_1 x). \tag{2.42}$$

It is possible to solve equations (2.36)-(2.40) in the linear case by assuming the ponderomotive force initially gives small variations in density so that the total electron density is written as $n_{\mathrm{e}} = 1 + \tilde{n}_{\mathrm{e}} \quad (\tilde{n}_{\mathrm{e}} \ll 1)$ where terms like $\frac{\partial \tilde{n}_{\mathrm{e}}}{\partial x}$

are small so that

$$\frac{\partial n_{\mathrm{e}}}{\partial t} = \frac{\partial \tilde{n}_{\mathrm{e}}}{\partial t} = -c\frac{\partial v_{\mathrm{e},x}}{\partial x}, \tag{2.43}$$

$$\frac{\partial v_{\mathrm{e},x}}{\partial t} = c\frac{\partial \phi}{\partial x} + c\frac{F_p}{m}, \tag{2.44}$$

$$\frac{\partial^2 \phi}{\partial x^2} = \frac{\omega_{\mathrm{p}}^2}{c^2}\tilde{n}_{\mathrm{e}}. \tag{2.45}$$

Taking the time derivative of equation (2.43) and inserting equation (2.44) gives

$$\frac{\partial^2 \tilde{n}_{\mathrm{e}}}{\partial t^2} = -c\frac{\partial^2 \tilde{v}_{\mathrm{e},x}}{\partial x \partial t} = -c^2\left[\frac{\partial^2 \phi}{\partial x^2} + \frac{\partial F_P}{\partial x}\right], \tag{2.46}$$

where inserting equation (2.45) into the equation above and rewriting yields

$$\frac{\partial^2 \tilde{n}_{\mathrm{e}}}{\partial t^2} + \omega_{\mathrm{p}}^2 \tilde{n}_{\mathrm{e}} = -2c^2 k_1^2 a_1 a_2 \cos(2k_1 x). \tag{2.47}$$

This equation is solvable by the assumption that the plasma is initially homogeneous, expressed through the initial conditions $\tilde{n}_{\mathrm{e}}|_{t=0} = 0$ and $\frac{\partial \tilde{n}_{\mathrm{e}}}{\partial t}|_{t=0} = 0$ which gives the final solution of the density variation of electrons

$$\tilde{n}_{\mathrm{e}} = -\frac{2k_1^2 c^2}{\omega_{\mathrm{p}}^2} a_1 a_2 \cos(2k_1 x)\left[1 - \cos(\omega_{\mathrm{p}} t)\right]. \tag{2.48}$$

From $\mathbf{E} = -\nabla\phi$ and equation (2.45) it is then possible to find the electric field and scalar potential by integration as

$$E_x = -k_1 a_1 a_2 \sin(2k_1 x)\left[1 - \cos(\omega_{\mathrm{p}} t)\right], \tag{2.49}$$

$$\phi = \frac{a_1 a_2}{2}\cos(2k_1 x)\left[1 - \cos(\omega_{\mathrm{p}} t)\right], \tag{2.50}$$

where E_x is normalised to mc^2/e. By inserting the induced electrostatic field into equation (2.38) and integrating one finds the ion momentum and in a similar way the electron momentum

$$p_{\mathrm{i},x} = k_1 c\frac{m}{M} a_1 a_2 \sin(2k_1 x)\left[t - \omega_{\mathrm{p}}^{-1}\sin(\omega_{\mathrm{p}} t)\right], \tag{2.51}$$

$$p_{\mathrm{e},x} = \frac{k_1 c a_1 a_2}{\omega_{\mathrm{p}}}\sin(2k_1 x)\sin(\omega_{\mathrm{p}} t). \tag{2.52}$$

Finally inserting the momentum into equation (2.39), introducing $n_{\mathrm{i}} = 1 + \tilde{n}_{\mathrm{i}} \quad (\tilde{n}_{\mathrm{i}} \ll 1)$ keeping only first order terms in the same way as for electrons, the ion density perturbation becomes

$$\tilde{n}_{\mathrm{i}} = -k_1^2 c^2 \frac{m}{M} a_1 a_2 \cos(2k_1 x)\left[t^2 - 2\omega_{\mathrm{p}}^{-2}\left(1 - \cos(\omega_{\mathrm{p}} t)\right)\right], \tag{2.53}$$

these expressions are equivalent to those given in [20, 22]. Equations (2.48) and (2.53) both have the same periodic spatial structure of period π/k_1, dependent only on the laser wavenumber in the plasma. For a $0.8\,\mu$m wavelength and homogeneous density of $n_0 = 0.3n_\mathrm{c}$ this corresponds to a spatial period of $0.478\,\mu$m. Additionally the ion density develops more slowly due to the scaling with mass as m/M. Considering an electron-proton plasma and laser intensities $a_1 = a_2 = 0.05$ (approximately corresponding to $I = 5 \cdot 10^{15}\,\mathrm{Wcm}^{-2}$ one finds from the condition ($\tilde{n}_\mathrm{e} \sim 1$) that the linear approximation is valid for times $t < 23\,\mathrm{fs}$.

2.6.2 Stationary Solution

As mentioned, to complement this linear approximation, it is possible to find a stationary solution for infinite plane waves. Recall that the cold plasma equation neglects the pressure term, in order to find the stationary solution it has to be re-introduced. Maximum density and the width of the peaks are a balance of three forces, the thermal pressure force acting as an outward push, the electrostatic force pulling particles of opposite charge together and the ponderomotive force pushing both electrons and ions into the troughs of the corresponding potential [30]. The pressure terms for electrons and ions are $\frac{1}{n_\mathrm{e}mc}\frac{\mathrm{d}P_\mathrm{e}}{\mathrm{d}x}$ and $\frac{1}{n_\mathrm{i}Mc}\frac{\mathrm{d}P_\mathrm{i}}{\mathrm{d}x}$ respectively, where $P_\alpha = n_\alpha k_\mathrm{B} T_\alpha$ and are introduced on the left hand sides of equations (2.36) and (2.38). The stationary assumption makes the terms $\frac{\partial p_\alpha}{\partial t} = 0$, giving

$$\frac{1}{n_\mathrm{e}mc}\frac{\mathrm{d}P_\mathrm{e}}{\mathrm{d}x} = c\frac{\partial(\phi - \bar{\gamma})}{\partial x}, \tag{2.54}$$

$$\frac{1}{n_\mathrm{i}Mc}\frac{\mathrm{d}P_\mathrm{i}}{\mathrm{d}x} = -c\frac{m}{M}\frac{\partial \phi}{\partial x}. \tag{2.55}$$

The spatial derivative of the temperature is neglected by assuming the electron bunching is an isothermal process, giving a first order linear ODE with solutions for $n_\alpha(x)$ given by

$$n_\mathrm{e} = C_1 \mathrm{e}^{\beta_1(\phi - \bar{\gamma})}, \tag{2.56}$$

$$n_\mathrm{i} = C_2 \mathrm{e}^{-\beta_2 \phi}, \tag{2.57}$$

where $\beta_1 = \frac{mc^2}{k_\mathrm{B}T_\mathrm{e}}$ and $\beta_2 = \frac{mc^2}{k_\mathrm{B}T_\mathrm{i}}$ and C_1 and C_2 are integration constants to be determined. From requiring quasi charge neutrality ($n_\mathrm{e} \simeq Zn_\mathrm{i}$) and equating exponents it is seen that

$$\phi = \frac{\beta_1 \bar{\gamma}}{(\beta_1 + \beta_2)}, \tag{2.58}$$

where $\bar{\gamma}$ is the known ponderomotive potential, giving

$$Zn_\mathrm{i} = n_\mathrm{e} = C\mathrm{e}^{-\beta\cos(2k_1 x)}, \tag{2.59}$$

where C is a new constant containing all components not spatially varying and $\beta = \frac{mc^2 a_1 a_2}{2k_\mathrm{B}T_\mathrm{e}(1+\frac{T_\mathrm{i}}{T_\mathrm{e}})}$. The final constant C is determined through conservation of particle number by assuming no particles are created or destroyed. This condition is given by a spatial integral over one period

$$1 = C\int_0^{\pi/k_1} \mathrm{d}x\, \mathrm{e}^{-\beta\cos(2k_1x)} = CI_0(\beta), \tag{2.60}$$

so that $C = 1/I_0(\beta)$ where I_0 is the modified Bessel function of the first kind of order zero. Equation (2.59) with this constant C is similar to that of [22] and equivalent to that found in [31]. Assuming temperatures $T_\mathrm{e} = 25\,\mathrm{eV}, T_\mathrm{e}/T_\mathrm{i} = 10$ and laser intensity $a_1 = a_2 = 0.05$ one gets $\beta \approx 23$ for which $1/I_0(\beta) \approx \sqrt{2\pi\beta}\mathrm{e}^{-\beta}$. With these considerations the density grating is that shown in Figure 2.3. Here the maximum density is approximately $12n_0$, which in simulations will be shown to be an overestimation by a factor three, in some part due to neglecting heating from the electrostatic field.

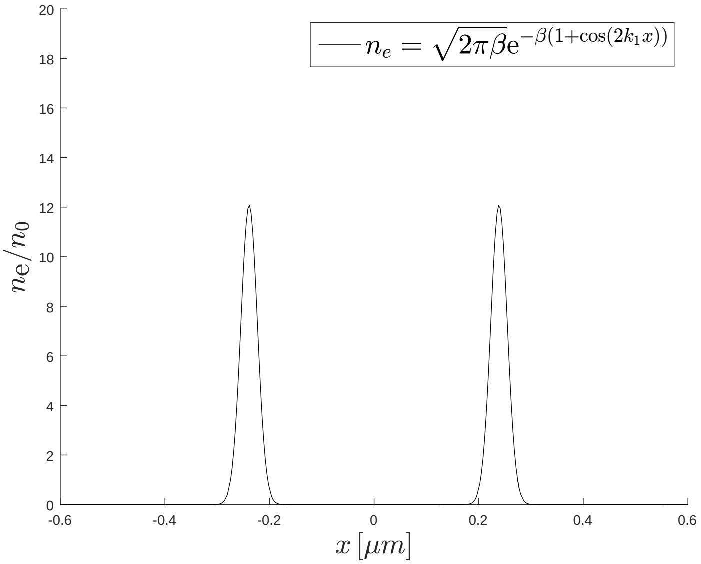

Figure 2.3: Stationary solution of electron density grating normalised to initial homogeneous density n_0, with temperature $T_\mathrm{e}/T_\mathrm{i} = 10$ and laser intensity $a_1 = a_2 = 0.05$.

2.6.3 Dispersion Relation for Periodic Structures

Similar to how in section 2.4, where it was shown that homogeneous plasmas can sustain propagating electromagnetic waves, this section describes the properties of waves in periodic dielectric structures. Assuming the wave incident on the periodic structure in Figure 2.3 is a transverse plane wave travelling along the $x-$axis it is possible to treat the problem using the wave equations derived in section 2.4

$$-\nabla(\nabla\cdot\mathbf{E})+\nabla^2\mathbf{E}+\frac{\omega^2}{c^2}\epsilon(\omega)\mathbf{E}=0, \tag{2.61}$$

$$\nabla^2\mathbf{B}+\frac{\omega^2}{c^2}\epsilon(\omega)\mathbf{B}=0. \tag{2.62}$$

Furthermore assume the wave is s-polarised*, $\mathbf{E}=E_z(\mathbf{r})\mathrm{e}^{\mathrm{i}\omega t}\mathbf{e}_z$, i.e. the electric field is perpendicular to the plane of incidence which is spanned by the two vectors of incident and reflected rays. This corresponds to solving equation (2.61) where inserting the field, noting the first term becomes zero, leaves us with

$$\left(\frac{\partial^2}{\partial x^2}+\frac{\partial^2}{\partial y^2}\right)E_z(\mathbf{r})+\epsilon(\omega,x)\frac{\omega^2}{c^2}E_z(\mathbf{r})=0, \tag{2.63}$$

where the dielectric function is now a function of both frequency and space due to the varying density since

$$\epsilon(\omega,x)=1-\frac{\omega_\mathrm{p}^2}{\omega^2}=1-\frac{n_\mathrm{e}(x)e^2}{\epsilon_0 m_\mathrm{e}\omega^2}. \tag{2.64}$$

To solve this equation one notes that the dielectric function is periodic in $L=\pi/k_1$ since $n_\mathrm{e}(x+L)=n_\mathrm{e}(x)$ and makes use of the Floquet-Bloch theorem [32, 33], which states that a wave solution subject to an infinitely periodic potential can be expressed as

$$E(\mathbf{r})=\mathrm{e}^{\mathrm{i}\mathbf{k}\cdot\mathbf{r}}u(\mathbf{r}), \tag{2.65}$$

where $u(\mathbf{r})$ is a function with the same periodicity as $n_\mathrm{e}(x)$ and $\mathbf{k}=(k_x,k_y,0)$ is called the Bloch wavenumber. Expanding $n_\mathrm{e}(x)$ and $u(\mathbf{r})$ in complex Fourier series gives

$$n_\mathrm{e}(x)=\sum_p \eta_p \mathrm{e}^{\mathrm{i}\frac{2\pi p}{L}x}, \tag{2.66}$$

$$u(\mathbf{r})=\sum_{\mathbf{b}_p} c_p(\mathbf{b}_p)\mathrm{e}^{\mathrm{i}\mathbf{b}_p\cdot\mathbf{r}}, \tag{2.67}$$

where $p\in\mathbb{Z}$ and $\mathbf{b}_p=(\frac{2\pi p}{L},0,0)$ are lattice vectors which only has an x-component since this is the only direction the density is periodic in. The Fourier coefficients of n_e normalised to n_0, applied to the stationary solution found in the previous section, are given by

$$\eta_p=\int_0^L \mathrm{d}x\, n_\mathrm{e}(x)\frac{\mathrm{e}^{-\mathrm{i}\frac{2\pi p}{L}x}}{L}=\int_0^L \mathrm{d}x\,\frac{\mathrm{e}^{-\beta\cos(2k_1x)}}{I_0(\beta)}\frac{\mathrm{e}^{-\mathrm{i}\frac{2\pi p}{L}x}}{L}=\frac{I_p(\beta)}{I_0(\beta)}, \tag{2.68}$$

where the $I_p(\beta)$ is the modified Bessel function of the first kind of integer order p [34, p. 376].

---

[*] The designation s-polarised stems from the German word *senkrecht*, meaning perpendicular, whereas p-polarised waves are parallel to the plane of incidence.

Inserting equations (2.64)-(2.67) into equation (2.63) and normalising so that $n_{\mathrm{e,unit}} = n_{\mathrm{c}}$, $t_{\mathrm{unit}} = \omega_0^{-1}$, $x_{\mathrm{unit}} = c/\omega_0$, and $E_{\mathrm{unit}} = \frac{m_{\mathrm{e}} c \omega_0}{e}$ yields

$$\begin{aligned}
&\sum_p c_p \left[\left(\frac{\partial^2}{\partial x^2} + \frac{\partial^2}{\partial y^2} \right) + \frac{\omega^2}{\omega_0^2} \right] \mathrm{e}^{\mathrm{i}(\mathbf{k}+\mathbf{b}_p)\cdot\mathbf{r}} - \\
&\qquad \sum_p c_p \mathrm{e}^{\mathrm{i}(\mathbf{k}+\mathbf{b}_p)\cdot\mathbf{r}} \sum_p \eta_p \mathrm{e}^{\mathrm{i}\frac{2\pi p}{L}x} = 0 \Rightarrow \\
&\sum_p c_p \left[-\left(k_x + \frac{2\pi p}{L} \right)^2 - k_y^2 + \frac{\omega^2}{\omega_0^2} \right] \mathrm{e}^{\mathrm{i}(\mathbf{k}+\mathbf{b}_p)\cdot\mathbf{r}} - \\
&\qquad \sum_p \left(\sum_{p'} \eta_{p-p'} c_{p'} \right) \mathrm{e}^{\mathrm{i}(\mathbf{k}+\mathbf{b}_p)\cdot\mathbf{r}} = 0
\end{aligned} \tag{2.69}$$

where the second term involving a product of two Fourier series has been rewritten using an identity for the convolution of Fourier coefficients. Next, requiring the coefficients to be zero then results in an infinite set of coupled equations [21]

$$c_p \left[-\left(k_x + \frac{2\pi p}{L} \right)^2 - k_y^2 + \frac{\omega^2}{\omega_0^2} \right] - \sum_{p'} \eta_{p-p'} c_{p'} = 0. \tag{2.70}$$

It is instructive to use the two band model through which assuming the first two coefficients $p = 0, -1$ are the most important it is possible to estimate the width of the first band gap by solving near the edge of the first Brillouin zone [35, p. 177]. For normal incidence of the waves ($k_y = 0$) equation (2.70) on matrix form for these two coefficients becomes

$$\begin{bmatrix} -k_x^2 - \eta_0 + \frac{\omega^2}{\omega_0^2} & -\eta_{-1} \\ -\eta_{-1} & -(k_x - \frac{2\pi}{L})^2 - \eta_0 + \frac{\omega^2}{\omega_0^2} \end{bmatrix} \begin{bmatrix} c_0 \\ c_{-1} \end{bmatrix} = \mathbf{0}. \tag{2.71}$$

Non-trivial solutions are found when the determinant of the 2×2 matrix is zero, giving the two solutions evaluated at the edge of the first Brillouin zone (gaps are generally expected at points of high symmetry, see e.g. [36, p. 31]) located at $k_x = k_1$ rather than $k_x = k_0$ due to the reduced wavenumber in the plasma

$$\frac{\omega_{1,2}}{\omega_0} = \sqrt{\frac{\pi^2}{L^2} + \eta_0 \pm \eta_{-1}}. \tag{2.72}$$

Assuming $n_0 = 0.3 n_{\mathrm{c}}$, the width of the band gap is then given by

$$\frac{\Delta\omega}{\omega_0} \approx \sqrt{\frac{\pi^2}{L^2} + \eta_0 + \eta_{-1}} - \sqrt{\frac{\pi^2}{L^2} + \eta_0 - \eta_{-1}} \approx 28\%, \tag{2.73}$$

similar to the expression in [21]. This procedure is easily repeated for other periodic variations in density, in particular those obtained from simulations.

Figure 2.4 shows the band structure including terms up to $p = \pm 4$ where it is clear the structure shows photonic band gaps, the largest of which is the first one at almost 30%. Solid lines correspond to propagating Bloch modes whereas dashed lines are the solutions with complex k_x which similarly to the case of cutoff frequency defined by n_c leads to exponentially decaying modes. The larger the amplitude of the $\mathrm{Im}(k_x)$ the faster the modes decay. Note that this has been shown for infinitely periodic plasmas, however with enough periods also finite structures should approximately reproduce this band diagram.

Since there is no structure along the y-axis oblique incidence ($k_y \neq 0$) allows continuum bands of propagating modes because for each allowed k_x it is possible to choose any k_y since these are not limited by any Bloch condition. Because of this continuum, a wave with oblique incidence can for some angles propagate even for frequencies corresponding to the middle of the band gap for normal incidence. The angle of incidence with respect to the normal of the grating surface is determined via $k_y/k_x = \tan(\theta)$.

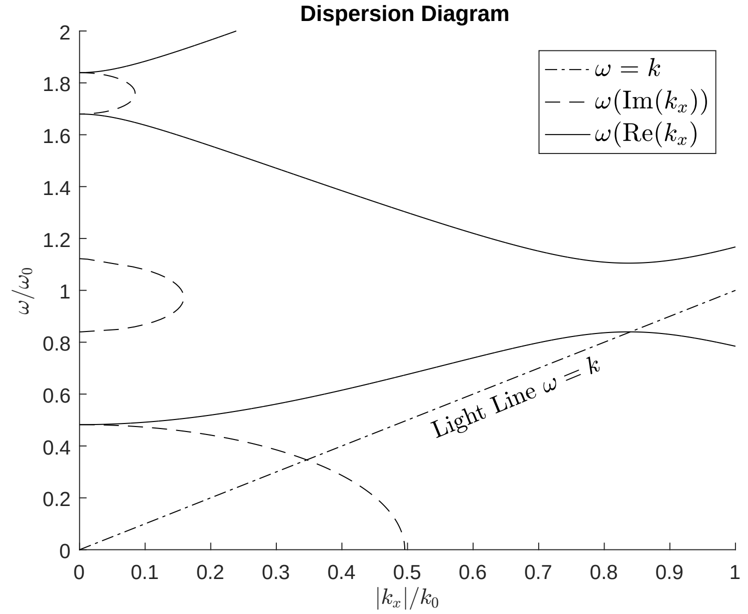

Figure 2.4: Real and complex band structure of the density grating obtained in the stationary approximation using temperature $T_\mathrm{e}/T_\mathrm{i} = 10$ and laser intensity $a_1 = a_2 = 0.05$ and initial density $n_0 = 0.3n_\mathrm{c}$ (for which the edge of first Brillouin zone is located at $k_x/k_0 \approx 0.836$).

Chapter 3

Slow Light

As mentioned previously, a dispersion relation gives insight into the propagation characteristics of the wave. This chapter briefly discusses the different types of effects which modify the propagation velocity of light, under what conditions these occur and some basic limitations.

3.1 Material Slow Light

Each wave is characterised by two different velocities. The first is the phase velocity which for transparent nondispersive media is simply defined by

$$v_{\mathrm{ph}} = \omega/k = c/n, \tag{3.1}$$

where ω is the frequency, k is the wavenumber, c is the speed of light in vacuum and n is the refractive index of the media. The second one is the group velocity, the speed at which an electromagnetic pulse propagates, defined by

$$v_{\mathrm{g}} = \frac{\partial \omega}{\partial k}, \tag{3.2}$$

which for nondispersive media is identical to the phase velocity.

Slow light is further divided into two subcategories, material and structural. Material slow light is the slowing of light in a uniform, dispersive medium where the refractive index is strongly frequency-dependent. In this case the phase velocity is defined in the same way and the group velocity can be shown to be [37]

$$v_{\mathrm{g}} = \frac{\partial \omega}{\partial k} = \frac{c}{n + \omega \frac{\mathrm{d}n}{\mathrm{d}\omega}}, \tag{3.3}$$

where it is common to define the group index as $n_{\mathrm{g}} = n + \omega \frac{\mathrm{d}n}{\mathrm{d}\omega}$. Since n is usually on the order of unity, the slow light is mainly governed by the speed at which the refractive index changes with frequency. This term can be both positive and negative, where the positive case gives slow light and the negative case is associated with fast light phenomena. In many cases, it can be shown that the group velocity is also the same as the velocity of energy transfer [38].

As an important example, consider the dispersion relation for electromagnetic waves in a homogeneous plasma derived previously, where the refractive index n becomes

$$n = \sqrt{1 - \frac{\omega_{\mathrm{p}}^2}{\omega^2}}. \tag{3.4}$$

In this case the phase and group velocities become

$$v_{\mathrm{ph}} = \frac{c}{\sqrt{1 - \frac{\omega_{\mathrm{p}}^2}{\omega^2}}}, \tag{3.5}$$

$$v_{\mathrm{g}} = c\sqrt{1 - \frac{\omega_{\mathrm{p}}^2}{\omega^2}}. \tag{3.6}$$

As the frequency approaches the cutoff frequency ω_{p} the phase velocity becomes infinite and the group velocity approaches zero. Note also that ω_{p} is dependent on the electron number density. The group velocity as a function of frequency for three different densities are shown in Figure 3.1, these curves are important as a comparison when investigating the second type of slow light, i.e. structural slow light.

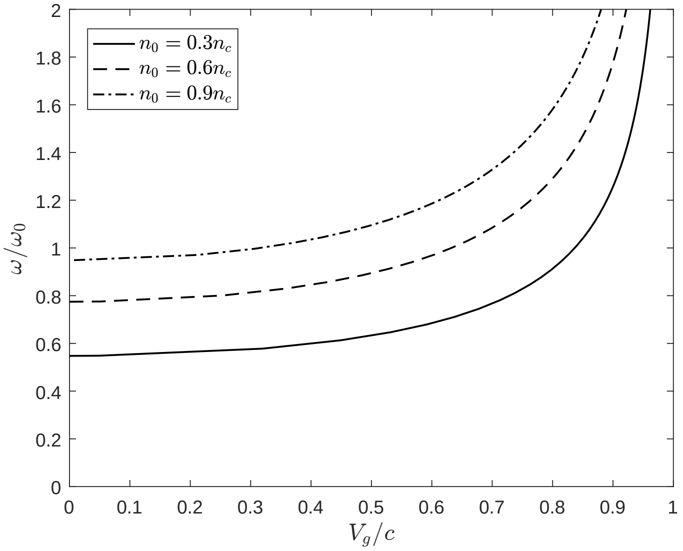

Figure 3.1: Group velocity in homogeneous plasma for different densities given by equation (3.6). The intersection with the y-axis is at $\omega = \omega_{\mathrm{p}}$.

3.2 Structural Slow Light

Structural slow light is fundamentally different to material slow light. As the name implies it is not the material properties, but rather the structure of the material, usually periodic crystals in one or more dimensions, which modifies the propagation of pulses. The most simple such photonic crystal is the periodic stack of two materials with different dielectric constant, a very similar system is that described in section 2.6, where the dispersion relation of a photonic crystal structure, consisting of a plasma density grating, with continuously varying dielectric function was shown. A heuristic explanation of the slow light origin in this case is that the pulse is partially reflected at each interface, making the average photon and thus the pulse envelope propagate through the crystal slower.

The speed of a light pulse in a dielectric structure is still described by $v_{\mathrm{g}} = \frac{\partial\omega}{\partial k}$, where k is now the Bloch wavenumber of the propagating mode [38]. Looking at the dispersion relation in Figure 2.4 it is easy to see the lower band close to the band gap gives rise to a slow light mode. The upper band is a bit more subtle. In this case the group velocity and phase velocity become anti-parallel, i.e. $v_{\mathrm{g}} < 0$ and $v_{\mathrm{ph}} > 0$, at first glance one might assume the negative slope must correspond to fast light as the pulse leaves the material before it enters. This is however not a complete picture as the dispersion relation displays reflection symmetry, so that for negative k_x the upper band instead has a positive slope near the band gap, giving instead $v_{\mathrm{g}} > 0$ and $v_{\mathrm{ph}} < 0$. A detailed discussion on how to determine which of these solutions is correct a priori is outside the scope of this thesis, but it has been argued that applying causality, only one solution is valid in each scenario [39].

3.3 Limitations

Finally, since an electromagnetic pulse is assumed finite in time it must contain a band of frequencies. This necessarily leads to a relation limiting how slow a pulse can propagate given some bandwidth [40]. To see this, let Δk be the range of Bloch wavenumbers and $\Delta\omega$ be the range of frequencies of the pulse. Under the assumption that

$$\Delta k < 2\pi/L, \tag{3.7}$$

where L is the periodicity of the crystal, and the assumption that the periodicity is of the order of a wavelength

$$L \sim \lambda_0 = 2\pi c/\omega, \tag{3.8}$$

one finds the average group velocity $\langle v_{\mathrm{g}} \rangle = \frac{\Delta\omega}{\Delta k}$ to be limited by

$$c\frac{\Delta\omega}{\omega} \sim \Delta\omega\frac{L}{2\pi} < \langle v_{\mathrm{g}} \rangle. \tag{3.9}$$

For example, a 30 fs Gaussian pulse with $\lambda_0 = 0.8\,\mu$m gives $\langle v_{\mathrm{g}} \rangle \gtrsim 0.04c$.

Chapter 4

Numerical Methods

4.1 PIC codes and EPOCH

In this chapter the simulation methods used in this thesis and the stability conditions required to run simulations of physical significance are described briefly. All simulations are run with the particle in cell (PIC) code EPOCH [41]. The core of any collisionless PIC algorithm is based on two coupled solvers, one solving Maxwell's equation called the field solver, and the other moving the charged particles under the influence of the electromagnetic fields, called the particle pusher.

Maxwell's equations are solved using the finite difference time-domain (FDTD) method on a fixed spatial grid. The E- and H-field components are defined on a staggered grid as introduced by Yee [42], although EPOCH supports use of several other field solvers. The positions in three dimensions are shown in Figure 4.1. This staggered grid makes central derivatives of **E**-field components second order accurate* at the positions where they are used to solve for the **H**-field components and vice versa.

Many PIC codes, including EPOCH, use a leapfrog method which solves the fields at full and half time steps. The half time-step values are needed for the particle pusher in order to make it second order accurate as well.

In the ideal case the particle pusher would solve the relativistic equation of motion for every single particle, this is however a computationally impossible task. To remedy this, each computational particle (CP) represents a large amount of real particles by using the sum of charges and currents of the real particles. Because of this CPs are often called super particles or macro particles. In the next chapter these will simply be referred to as particles when specifying how many particles have been used per cell in a simulation.

---

*A numerical solution is called n:th order accurate when the error of the solution, $\mathscr{E}$, is proportional to the step size to the power n, i.e. $\mathscr{E} \propto (\Delta\alpha)^n$. Here, $\Delta\alpha$ is either the time step or spatial step size.

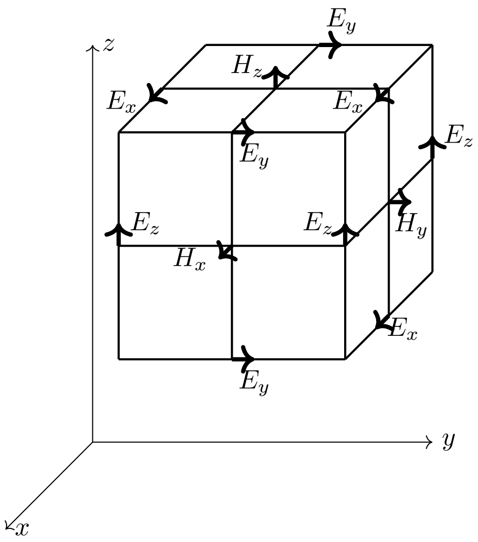

Figure 4.1: The staggered positions of E and H fields on a 3D cell [43].

The particle pusher in EPOCH uses a leapfrog method, calculating the momentum and position at alternating half time-steps which, as mentioned, is why the fields are needed at half time-steps. From the particle motions the current densities needed for Maxwell's equations are then obtained through the flux of charge, as opposed to calculating it from the moments of the distribution function as is done in some other PIC codes.

The particles are free to move in a continuum space, that is, they are not defined on nodes as the fields are. This introduces the issue of determining how much of the current density of a particle should be used to update the fields at the closest lying nodes. Figure 5.3 shows in the two dimensional case how the charge is assigned to grid points. For example, the point labelled B is assigned the amount of charge proportional to the area b, logically since the particle is closest to B, this point is assigned most of the charge. Clearly, the fields need to be interpolated to the positions of particles in a similar way. Figure 4.3 contains a flow chart of the most basic four steps of a PIC code, after initialisation the charge is interpolated to the grid to calculate the fields. The fields are then interpolated to the particle positions to calculate the new velocities and positions.

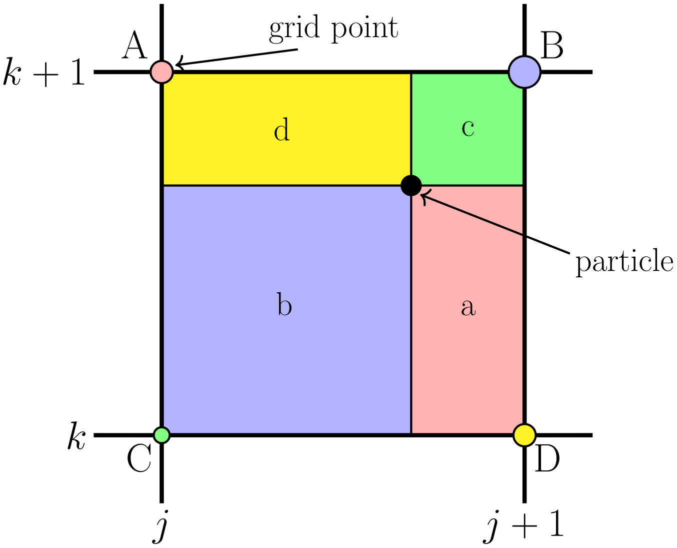

Figure 4.2: Linearly weighted charge assignment in the PIC bilinear interpolation interpretation [44]. The sizes of the circles denote the relative amount of charge of the particle which is deposited to each grid point and the colours denote the corresponding area.

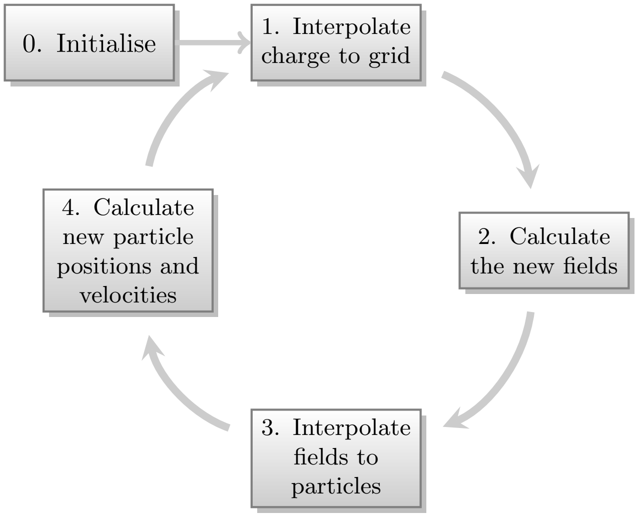

Figure 4.3: The basic four steps of the coupled solvers in a PIC code.

There are several stability conditions to take into consideration when using PIC codes. The most fundamental as with any partial differential equation solved using the finite difference method is the CFL condition, given in two dimensions by (see e.g. [45] for a detailed derivation)

$$\Delta t \leq c^{-1}\left(\frac{1}{(\Delta x)^2}+\frac{1}{(\Delta y)^2}\right)^{-1/2}, \tag{4.1}$$

where Δx and Δy are the grid spacings in the x and y directions and Δt is the time step, or in one dimension, letting $\Delta y \to \infty$, giving $\Delta t \leq \Delta x/c$. When the spatial resolution in all directions is the same, $\Delta x = \Delta y = \Delta$, this condition takes its simplest form

$$\Delta t \leq \frac{\Delta}{c\sqrt{2}}. \tag{4.2}$$

In principle, when interested in simulating a travelling wave, the CFL condition describes the necessity to have a time step so small that the travelling wave does not have time to propagate to a new grid point during the time of a single time step.

The other stability conditions are defined from the fundamental time and length scales as given in section 2.2 and 2.3. In order to have a physically correct picture it is necessary to have $\Delta t \leq 2\omega_\mathrm{p}^{-1}$ however even smaller time steps are recommended to avoid instabilities such as self heating, where instead $\Delta t \leq 0.1\omega_\mathrm{p}^{-1}$ [46]. The other condition is related to the Debye length, suggesting that it is necessary to resolve it in order to avoid potentially large self heating, thus $\Delta x \sim \lambda_\mathrm{D}$ approximately, but this is not as strict as the other conditions. In short, self heating is a numerical instability where energy is not conserved and increases approximately linearly over time. To reduce self heating in EPOCH it is possible to use higher order shape functions. With the most simple shape function the charge of a computational particle is distributed in a top-hat (0th order b-spline) distribution in space, by default EPOCH uses a triangle (1st order b-spline) but higher order b-splines can be used as well. A detailed study of the effects of shape functions in EPOCH is included in [41].

Chapter 5

Results and Discussion

In this chapter the PIC simulation results of the formation of TPPCs by counterpropagating femtosecond laser pulses and the allowed angles of transmission are presented, confirming and expanding on earlier work by [20–22]. The results of the slow light properties of the TPPCs are also presented.

5.1 Formation of TPPCs

The formation of the density grating was first obtained in the one-dimensional case where a short $5\,\mu$m, fully ionised electron-proton plasma (masses $m_\mathrm{i} = 1836.2 m_\mathrm{e}$) of initially homogeneous density $n_{\mathrm{e},0} = n_{\mathrm{i},0} = 0.3 n_\mathrm{c}$ with $1.5\,\mu$m long Gaussian tails decaying to $n_\alpha = 0$ on each side was irradiated by two counterpropagating Gaussian pulses of intensities $a_1 = a_2 = 0.05$. The pulses were 300 fs long and reached the centre of the plasma simultaneously, creating a standing wave expanding from the centre outwards. The electron temperature T_e was 25 eV and the ion temperature T_i was 2.5 eV. The Debye length was resolved by letting the grid spacing be $\Delta x = 1\,\mathrm{nm}$. Because the simulation was one dimensional a high number of particles per cell could be used, set to 1000 for each species. The choice of density is motivated by the need for near critical density plasma to produce gratings with large photonic band gaps. The temperatures are chosen based on temperatures found in near critical density materials [23].

Figure 5.1 shows the electron density as a function of time near the centre of the plasma, displaying how two of the density peaks evolve. Three different times are indicated in the figure, $T_1 = 175\,\mathrm{fs}$ is the time when the two counterpropagating pulses begin forming the standing wave and $T_2 = 475\,\mathrm{fs}$ mark the time the pulses have propagated through the plasma. The time $T_3 = 675\,\mathrm{fs}$ is the time when the grating is maximally developed. Between T_1 and T_2 an electrostatic field E_x is formed as described in section 2.6.

The pulses overlapped long enough for the ions to gain enough momentum to drive the formation of the density grating even after the electrostatic field had vanished. The peaks obtained a maximum density of almost $1.4n_\mathrm{c} \approx 4.5n_0$ while the lowest density observed between the peaks was $0.1n_\mathrm{c}$, giving a density contrast factor of 14. The density grating obtained in the stationary solution in the theory clearly overestimated the results, mostly because of neglecting temperature, this can be seen from Figure 5.2 where the electron temperature across the two peaks is shown. Setting the electron temperature to 100 eV in the stationary solution to account for the heating gives a maximum density of $n_\mathrm{e} = 4n_0$, making the theoretical density grating match that of the simulation quite well. The periodicity of the grating $L \approx 480\,\mathrm{nm}$ is half the wavelength of the laser in the plasma, corresponding to the intensity troughs of the standing wave. The peak width is approximately $L/6$, also agreeing well with the stationary solution. Meanwhile, the maximum density variation predicted by the linear theory is

$$\tilde{n}_{\mathrm{e,max}} = \frac{2k_1^2c^2}{\omega_\mathrm{p}^2}a_1a_2 = 5\cdot 10^{-3}n_\mathrm{c}, \tag{5.1}$$

which is far below the simulated values. Note that the driving pulses are not greatly affected by the density variations as they have already propagated through the plasma before these build up to considerable levels.

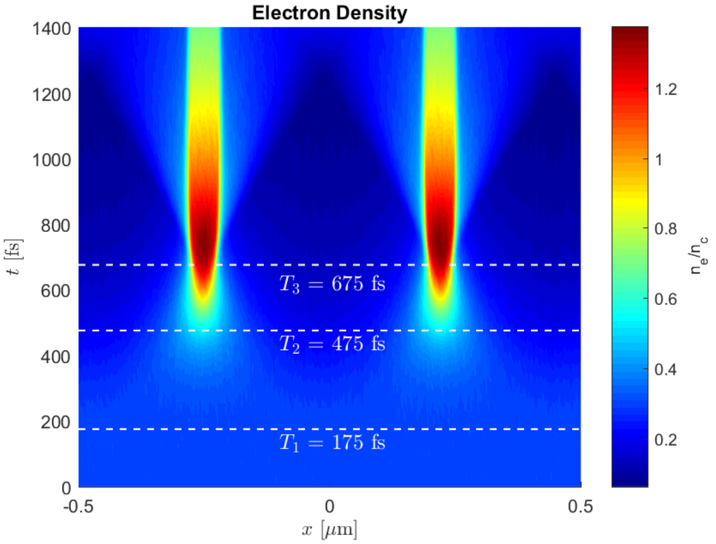

Figure 5.1: Two periods of the electron density grating showing peaks forming over time. Driving pulses overlap between T_1 and T_2 and the density reaches its maximum at T_3.

The maximum electrostatic field observed in the simulation as a result of the overlapping pulses was $E_x \approx 1\cdot 10^{10}\,\mathrm{Vm^{-1}}$, which can be compared to that calculated in the linear case where the maximum electrostatic field is given by

$$E_{x,\mathrm{max}} = k_1 a_1 a_2 = k_0 a_1 a_2 \sqrt{1 - n_{\mathrm{e},0}/n_{\mathrm{c}}} \tag{5.2}$$

where E_x was normalised to $e/m_\mathrm{e}c^2$. Inserting the values used in the simulation gives $E_{x,\mathrm{max}} \approx 8.4 \cdot 10^9\,\mathrm{Vm}^{-1}$, in good agreement with the simulation.

The linear model gives particle velocities as well which allows to estimate the maximum ion velocity and time to build the grating,

$$v_{\mathrm{i,max}}/c \sim k_1 c \frac{m}{M} a_1 a_2 \tau_\mathrm{L} = 8 \cdot 10^{-4}, \tag{5.3}$$

for $\tau_\mathrm{L} = 300\,\mathrm{fs}$ as used in the simulation. The ions are accelerated towards the nearest peak, on an average distance $L/4$ away ($L = 478\,\mathrm{nm}$ using the parameters from the simulation) which means they reach the centre of the peak at the latest $T = \frac{L}{4v_{\mathrm{i,max}}} = 500\,\mathrm{fs}$ after T_2. From Figure 5.3 the time is instead just 200 fs, but accounting for translation of protons between T_1 and T_2 the linear model gives a quite good approximation of the time for the grating to form.

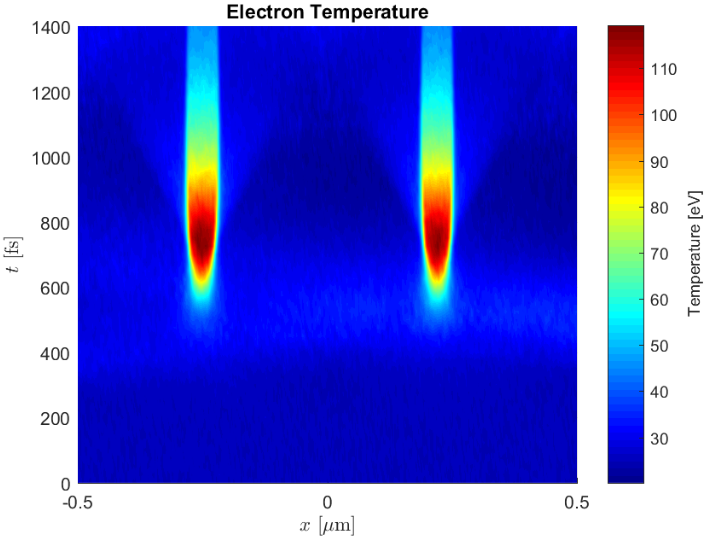

Figure 5.2: Electron temperature over two periods of plasma grating over time.

Figure 5.3 shows the deviation from charge neutrality in the same simulation by plotting $Zn_\mathrm{p} - n_\mathrm{e}$. During most of the simulation the protons follow the electrons to preserve charge neutrality, between T_1 and T_2 when the laser pulses overlap there is a slight surplus of electrons around where the peaks eventually form. After T_2 charge neutrality is quickly restored but once the fastest protons, accelerated by the electrostatic field, have reached the peaks slightly before T_3

and continued their ballistic trajectory into the centre of the peak a charge density mismatch forms. Two sheets of local electron dominance form on the sides of each peak and a bulk proton surplus is seen at the centre of the peak, quickly splitting into two sheets next to the electron sheets.

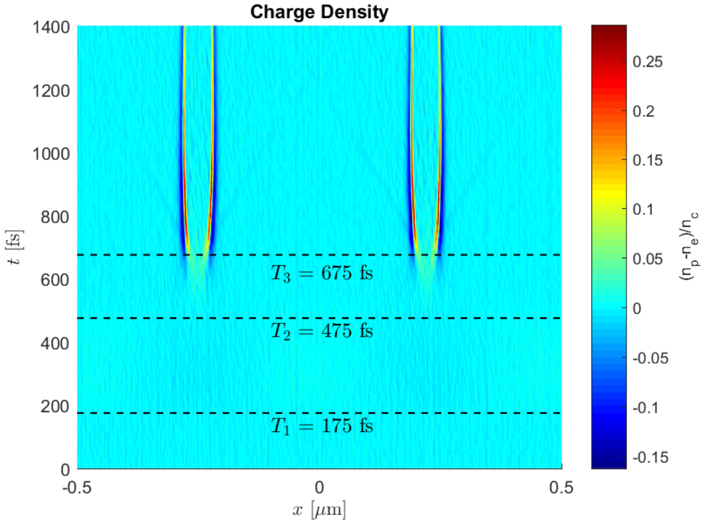

Figure 5.3: Charge density over two periods of plasma grating over time. Driving pulses overlap between T_1 and T_2 and the density reaches its maximum at T_3. Negative values correspond to negative charge surplus and positive values positive charge surplus.

In Figure 5.4 the phase space of electrons and ions is shown over a single period of the density grating shortly after the grating has developed fully, at time $T = T_2 = 475\,\text{fs}$. Electrons have already started to bunch up at the peak centre and the rest are slowly approaching with velocities of below $0.01c$. The protons have a Maxwellian velocity distribution and have reached their maximum velocity of $8 \cdot 10^{-4}c$ which is identical to the maximum ion velocity found in the linear approximation. Similarly electron velocity is seen to be of magnitude $2 \cdot 10^{-2}c$, larger than the estimated value of $4 \cdot 10^{-3}$ by almost one order because the electron velocity is strongly influenced by the temperature.

Figure 5.5 shows the same phase spaces at a later time $T = 690\,\text{fs}$, shortly after the maximum density has developed. Electrons are seen to be mostly confined to the peak and higher temperatures have made the maximum velocity increase slightly to around $0.045c$. The protons at this time have now also been confined to the peak, with protons on both sides still travelling towards the centre. The thin spike present on each side is initially a result of the fastest protons which were not stopped in the peak and continued their ballistic trajectory away from the peak. When the charge sheets in Figure 5.3 form, an electric field is induced (seen in Figure 5.6). This electric field acts to deflect incoming protons and also pull protons out of the peak [21], which leads to further decay of the peaks. The maximum proton velocity of $\max v_\mathrm{i} \approx 8 \cdot 10^{-4}$ is still the same as there are no accelerating forces left after T_2.

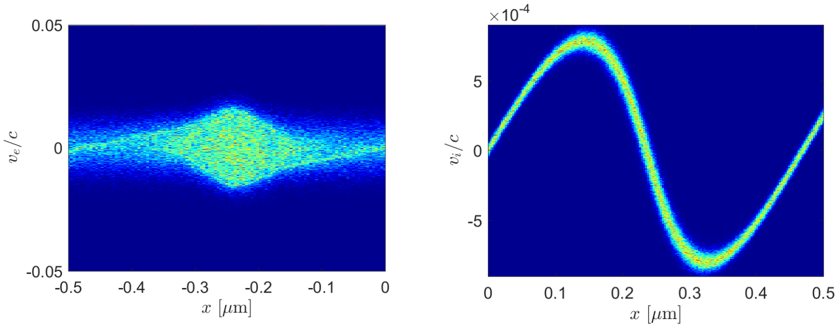

Figure 5.4: Phase space (x, v_x) of electrons (left) and protons (right) around the same two peaks as in Figure 5.1 at the time $T = T_2 = 475\,\mathrm{fs}$, when the driving pulses have propagated through the plasma.

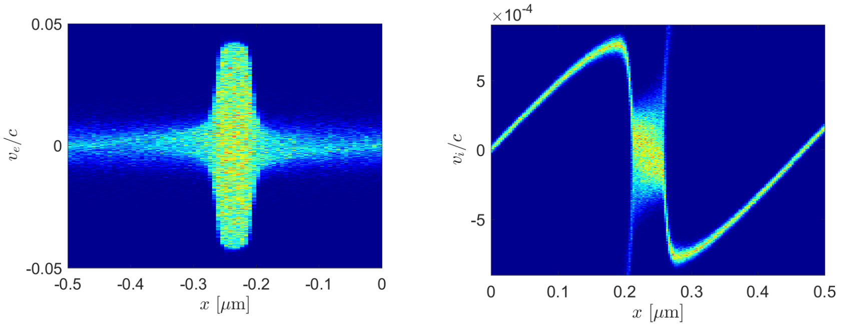

Figure 5.5: Phase space (x, v_x) of electrons (left) and protons (right) around the same two peaks as in Figure 5.1 at the time $T = 690\,\mathrm{fs}$, shortly after the maximal density has developed.

Figure 5.6 shows a cross section of the two peaks at time $T = 690\,\mathrm{fs}$ where in the left panel the electron density is shown and in the right panel the proton density is shown. The electric field across the two periods is also shown in units of $10^{11}\,\mathrm{V/m}$. The electron and proton density minima are seen to be equal at slightly above $0.1 n_\mathrm{c}$. The proton density spikes formed around the electric field are seen on the edges of the density peak. The sheets of electron surplus are more difficult to see, they come from the fact that the electron peak is slightly wider. The reason for the wider electron distribution is the difference in temperature ($T_\mathrm{e} > T_\mathrm{i}$) leading to increased thermal pressure which expands the peak. In simulation where $T_\mathrm{e} = T_\mathrm{i}$ the peak charge density is a factor 20 smaller, around $0.01n_\mathrm{c}$.

The electric field is as high as $0.4 \cdot 10^{11}$ V/m which is about four times larger than the electrostatic field present during the time the laser pulses overlapped.

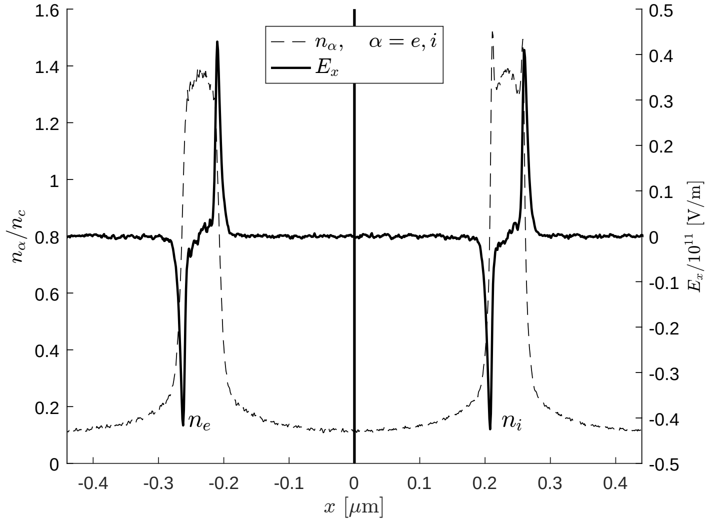

Figure 5.6: Cross section of two central peaks of the density grating at the time $T = 690$ fs when the electron sheets have formed. The electron density (left, dashed line) and proton density (right, dashed line). The electrostatic field E_x is also shown across both peaks (solid line).

The stationary solution predicts a strong dependence of the density peak height on the temperature of the plasma. Furthermore, plasma temperatures can vary experimentally depending on for example target material and time after plasma creation. Thus it is of interest to study the effects of temperature on the grating formation. Figure 5.7 shows how the maximum density evolves over time for four different temperatures, $T_\mathrm{e} = 5\,\mathrm{eV}, 10\,\mathrm{eV}, 25\,\mathrm{eV}$ and $50\,\mathrm{eV}$. In each case the ion temperature is $T_\mathrm{i} = T_\mathrm{e}/10$. Everything else except for the plasma length and simulation box size is identical to the previous simulation. The larger simulation box is the reason the peak density appears slightly later at $T \approx 800$ fs.

In all four simulations the initial build up proceeds identically until around 650 fs. The temperature dependence is clear, for higher initial temperatures the outward thermal pressure in the peaks becomes larger and acts to widen them, leading to lower maximum density. The highest obtained peak however, occurs mostly at the same time, with just a slight delay for lower temperatures. The above results are in excellent agreement with previous studies of the development of the density gratings using Maxwell-Vlasov codes in [20, 21].

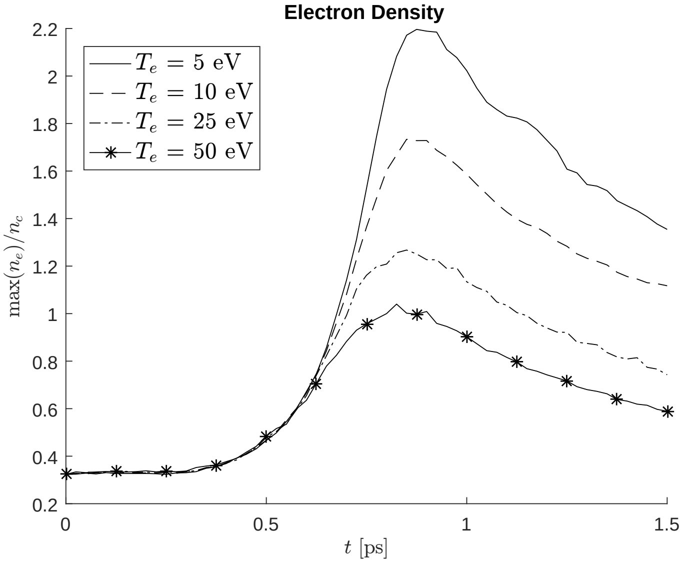

Figure 5.7: Temporal evolution of the maximum peak density of a plasma grating for different electron temperatures, $T_\mathrm{e} = 5\,\mathrm{eV}$ (solid line), $10\,\mathrm{eV}$ (dashed line), $25\,\mathrm{eV}$ (dash-dotted line) and $50\,\mathrm{eV}$ (solid line with stars). In each case the ion temperature is given by $T_\mathrm{i} = T_\mathrm{e}/10$.

As producing materials of near critical densities can be challenging, the effect of initial density was studied. Figure 5.8 shows how the maximum peak density evolves over time given different initial densities $n_{\mathrm{e},0} = 0.01n_\mathrm{c}, 0.05n_\mathrm{c}, 0.1n_\mathrm{c}$ and $0.3n_\mathrm{c}$. The overall dynamics of the grating do not change drastically, but in each case the maximum density is $n_{\mathrm{e,max}} \approx 4n_0$. Since the dielectric constant was found to be dependent on density this means a low initial density will give a small variation in dielectric constant and as a result the photonic crystal will have a small or nonexistent band gap.

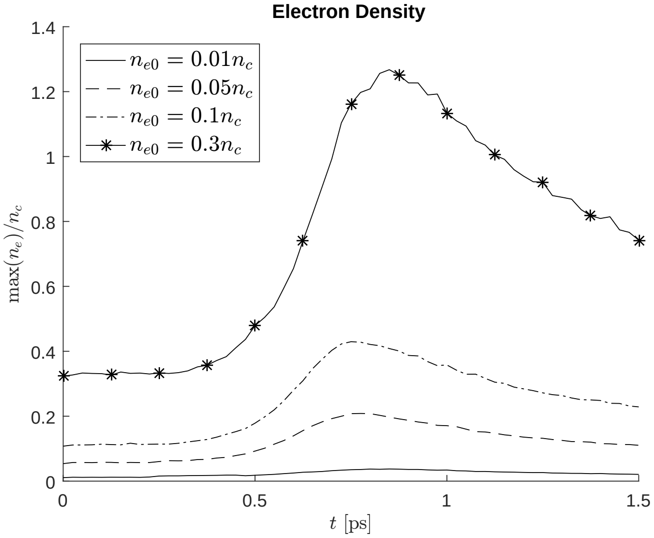

Figure 5.8: Temporal evolution of the maximum peak density of a plasma grating for different initial densities, $n_{\mathrm{e},0} = 0.01n_{\mathrm{c}}$ (solid line), $0.05n_{\mathrm{c}}$ (dashed line), $0.1n_{\mathrm{c}}$ (dash-dotted line) and $0.3n_{\mathrm{c}}$ (solid line with stars).

Since laser power is limited in experiments, it is of interest to find the minimum required energy in the driving pulses. Reducing the intensity of the driving pulses and keeping everything else the same has two effects, first the maximum density is reduced because the ponderomotive force becomes weaker, second because the ponderomotive force is weaker the overall dynamics is also slower. The result is longer lasting but weaker gratings. For higher intensities the result is the opposite, short lived gratings with higher peak density.

Another aspect of the energy needed used to establish a density grating is the driving pulse length. The length of the desired grating acts as a lower limit because at the very least the pulses need to overlap across the entire region. Figure 5.9 shows an example of this, where a $40\,\mu$m plasma of density $0.3n_{\mathrm{c}}$ was irradiated with two Gaussian driving pulses of intensity $a_1 = a_2 = 0.05$ and temperature $T_{\mathrm{e}} = 25\,\mathrm{eV}$, with $T_{\mathrm{i}} = T_{\mathrm{e}}/10$. The plasma consisted of electrons and protons ($m_{\mathrm{i}} = 1836.2m_{\mathrm{e}}$. The gratings obtained for four different driving pulse lengths are shown (symmetric about $x = 0$). For $\tau_{\mathrm{L}} = 100\,\mathrm{fs}$ FWHM the pulses clearly do not cover the entire plasma. With $\tau_{\mathrm{L}} = 200\,\mathrm{fs}$ the entire plasma is covered but ions located more than $10\,\mu$m from the plasma centre are not accelerated enough to produce an even grating. For $\tau_{\mathrm{L}} = 300\,\mathrm{fs}$ an even grating is formed across the entire plasma, note that the midsection has not increased beyond $n_{\mathrm{e,max}} \approx 1n_{\mathrm{c}}$. Further increasing the driving pulse duration leads to higher density peaks on the edges.

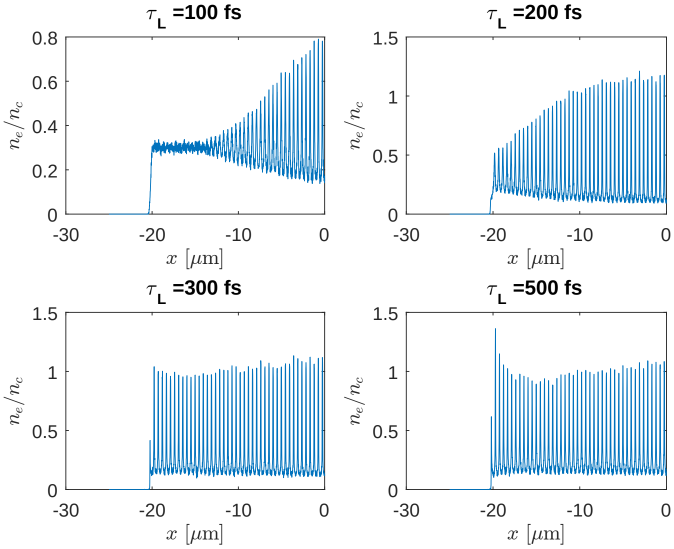

Figure 5.9: Electron density gratings formed by pulses of different lengths to illustrate convergence of the structure. Each grating is symmetric about $x = 0$. Clockwise from top left the gratings correspond to pulse lengths $\tau_{\mathrm{L}} = 100\,\mathrm{fs}, 200\,\mathrm{fs}, 500\,\mathrm{fs}$ and $300\,\mathrm{fs}$.

Another important practical consideration is the effect of chirped driving pulses on the formation of the grating. High power lasers use chirped pulse amplification where a short pulse is first stretched, also obtaining a chirp, then passed through some gain medium to increase the energy. Finally, the pulse is compressed again, reducing the chirp and producing an ultra high intensity pulse. One way to generate the required $\sim 2 - 300\,\mathrm{fs}$ driving pulses could then be to not compress the pulse fully. This leaves the driving pulses with a chirp. Figure 5.10 shows the grating produced in a $20\,\mu\mathrm{m}$ plasma around the times when the plasma grating has reached its maximum density contrast under the effects of two $200\,\mathrm{fs}$ driving pulses with a linear chirp corresponding to the spectral width of a $30\,\mathrm{fs}$ pulse. The intensity and temperatures are the same as those previously used.

It is evident that the maximum density has decreased slightly at the centre peaks, however the most important feature is the widening of the peaks as a result of the wavelength mismatch. As one might expect the mismatch is greater further out from the centre. As a result of this there is a limit to how large TPPCs with relatively even features can be created using uncompressed pulses from typical ultra high intensity laser setups. Of course, as previously discussed, reducing the width of the plasma in turn requires shorter pulses to have an overlap of sufficient time to create an even grating, which means driving pulses with less chirp can be used.

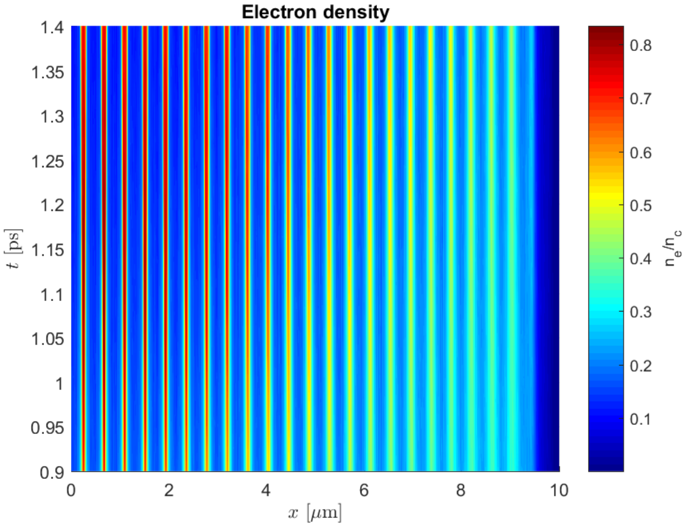

Figure 5.10: Electron density grating formed in a 20 μm plasma (symmetric around $x = 0$) using 200 fs pulses with a linear chirp corresponding to the spectral width of a 30 fs pulse. The grating is shown only during the times when it is fully developed.

5.2 Photonic Crystal Properties

In this section the photonic crystal properties of the density gratings are presented as obtained by PIC simulations, in particular the slow light properties are presented as a function of both frequency and angle of incidence.

The band structure was calculated using the same method of Bloch wave expansion as in the analytic example in section 2.6, but with the values for $n_{\mathrm{e}}(x)$ needed to calculate the Fourier coefficients η_p instead obtained from the density in the simulation. Note that this assumes an even density grating with enough periods to act as a quasi-infinite periodic structure. Figure 5.11 shows the band structure calculated from the grating in Figure 5.1 using $|p| \leq 3$ at $T = 650$ fs. The left side shows the case real and complex band structure for normal incidence, i.e. $k_y = 0$. The result is unsurprisingly more or less identical to the analytic band structure, with the only difference being the smaller band gap and smaller complex amplitude due to lower peak density.

The right side shows the projected band structure for $k_y \neq 0$, the boundary cases $\mathbf{k} = (0, k_y)$ and $\mathbf{k} = (k_1, k_y)$ are indicated in thick black and thin grey lines respectively. The shaded region between these mark a continuum of allowed states. As discussed in the theory these are a result of the grating only being structured along the x-axis. This is also the reason the band diagram is not periodic in k_y.

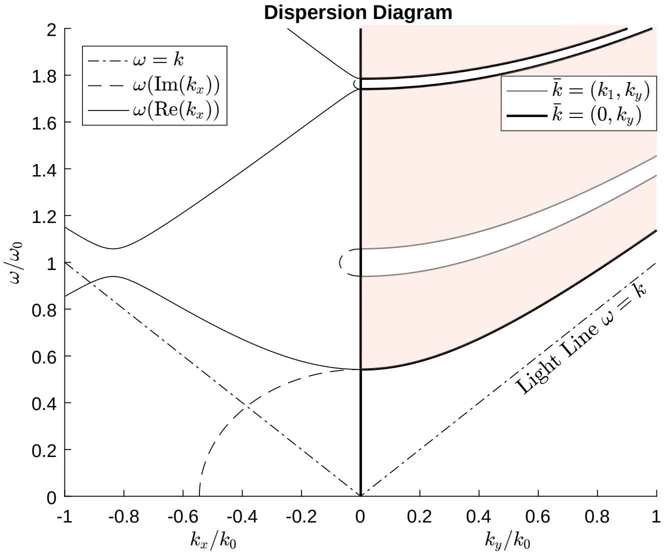

Figure 5.11: Band structure of the grating in Figure 5.1 calculated using the method of Bloch wave expansion at $T = 650\,\mathrm{fs}$. Left shows normal incidence band structure for real k_x (solid line), imaginary k_x (dashed line). Right shows projected oblique incidence band structure (shaded) and in particular $\mathbf{k} = (0, k_y)$ (black thick line) and $\mathbf{k} = (k_1, k_y)$ (grey thin line). Light line (dash dotted) is present on both sides.

As the dielectric function is density dependent, so is the band gap. Figure 5.12a shows how the Fourier coefficients η_p of order $p = 1, 2, 3$ of the grating in Figure 5.1 evolve over time. Initially only the first order is important. As the grating forms higher order coefficients become important.

Figure 5.12b displays the time dependence of the first band gap of the same grating. As higher order coefficients grow the band gap becomes slightly asymmetrical around ω_0. Note that the largest band gap does not correlate with the time where the highest density is found, but rather as a function depending on a combination of peak width and average density across the peak is the highest (around $T = 900\,\mathrm{fs}$).

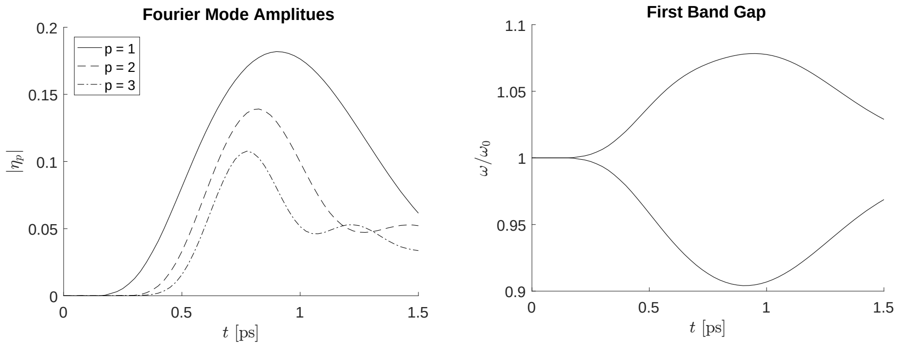

(a) Time dependence of first few Fourier coefficients.

(b) Time dependence of the first band gap located at $\omega/\omega_0 = 1$. Note the asymmetry due to higher order Fourier coefficients.

Figure 5.12

The band gap of the finite structure is simple to test by sending in a short pulse and observing the frequency response. Here, a 10 fs Gaussian pulse with normal incidence and a wavelength $\lambda = 0.8\,\mu$m was used. The pulse arrived at the grating at approximately $T = 675$ fs. The result is shown in Figure 5.13. The band gap is evident and closely resembles the theoretical first band gap at the corresponding time.

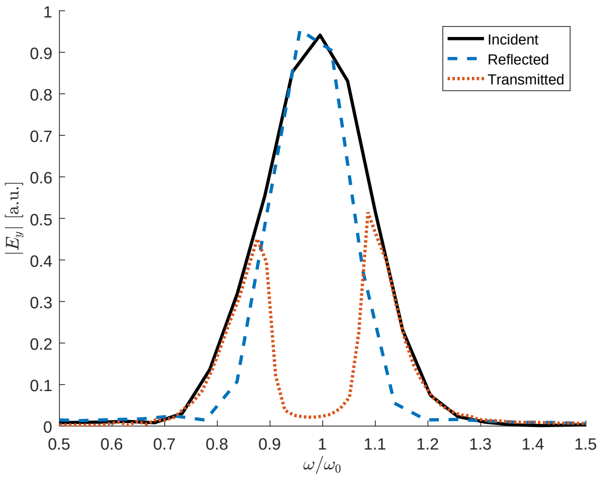

Figure 5.13: Incident spectrum (black solid line), reflected spectrum (blue dashed line) and transmitted spectrum (dotted orange line) of a 10 fs pulse.

Another important practical aspect is that of ion masses and their effects on the photonic crystal properties. Whether the method used to produce near critical plasmas is by low density foams as in [23] which use a combination of heavier elements (e.g. $C_{15}H_{20}O_6$) or by high pressure gas jets (where hydrogen is not optimal due to safety concerns), the effect of ion mass is of some importance.

Because of this, simulations as those previously described but with ions of mass $m_\mathrm{i} = 8m_\mathrm{p}$, where m_p is the proton mass, were carried out. Both the linear theory and stationary theory predict identical results, which one would expect as the charge to mass ratio remains the same, hence acceleration by the electrostatic field should not differ. In broad terms the results are more or less the same, however the grating is observed to develop more slowly and the peak density is reduced slightly from $1.4n_\mathrm{c}$ to $1.1n_\mathrm{c}$. For brevity only the Fourier modes and first band gap are presented in this case in Figure 5.14a and Figure 5.14b. The Fourier coefficients are seen to be reduced, in particular higher order coefficients. This in turn reduces the band gap width and the asymmetry vanishes. The band gap also develops slower and lasts longer.

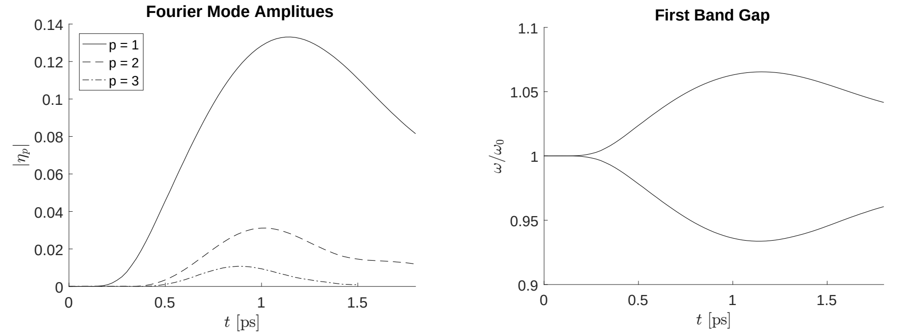

(a) Time dependence of first few Fourier coefficients for a plasma consisting of ions with mass $m_\mathrm{i} = 8m_\mathrm{p}$.

(b) Time dependence of the first band gap located at $\omega/\omega_0 = 1$ for a plasma consisting of ions with mass $m_\mathrm{i} = 8m_\mathrm{p}$.

Figure 5.14

Next, the group velocity of pulses travelling through density gratings were investigated in one dimension. A grating of length 50 μm identical to those previously described was obtained and Gaussian probe pulses of 70 fs FWHM arrived at the grating at a time when the analytic band structure closely resembled that in Figure 5.11 with $k_y = 0$, when the band gap is still symmetric around ω_0. From the theory, the relation $v_\mathrm{g} = \frac{\partial\omega}{\partial k}$ indicates that slow light should appear near the band gap at the edge of the first Brillouin zone where the derivative becomes zero. In light of this, the central frequency of the pulse was varied from $\omega/\omega_0 = 0.82$ to $\omega/\omega_0 = 1.18$ and the group velocity was determined from the velocity of the peak of the pulse envelope.

Figure 5.15 shows the results, marked by crosses for different frequencies, compared to the theoretical group velocity obtained from calculating the absolute value of the slope of the dispersion relation. The simulation is in excellent agreement with theory and for the pulse centred on $\omega = 1.08\omega_0$ the group velocity is found to be as low as $0.43c$. Note that the absolute value of the derivative, $|\frac{\partial\omega}{\partial k}|$, is used in the plot. As mentioned in chapter 3, this gives the velocity of the envelope of the pulse when the fast light mode is not causal.

The results of v_g should be compared to the numerical accuracy of the code as discretisation leads to numerical dispersion relations with errors depending on the spatial and temporal step sizes [45]. To test the accuracy the group velocity of a pulse in a vacuum region and homogeneous plasma were simulated. The obtained light speed in vacuum and homogeneous plasmas were both within 0.25% of the true speed using the same spatial and temporal step sizes as in the simulation of the propagation through the density grating.

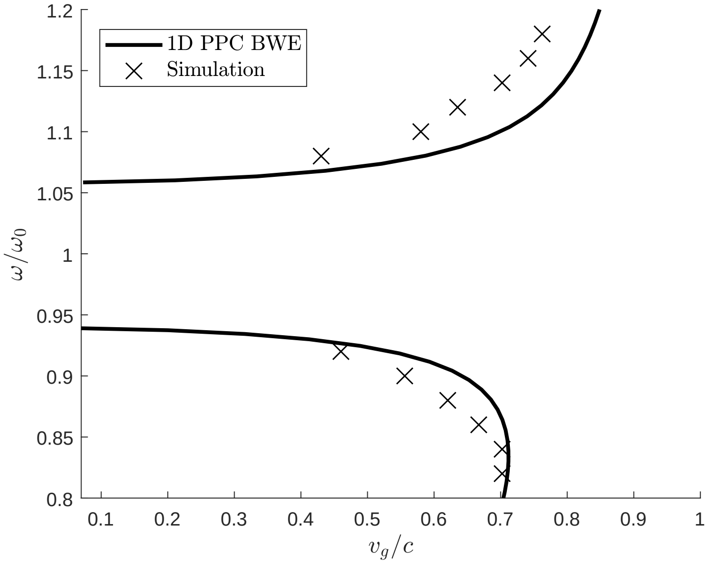

Figure 5.15: Group velocity versus frequency across the band gap. The thick black line is obtained by calculating $|\frac{\partial\omega}{\partial k}|$ of the dispersion diagram in Figure 5.11 for the case $k_y = 0$ (normal incidence). Crosses mark the group velocity observed in PIC simulations of 70 fs pulses with different frequencies.

Another consideration to make is the effective slow down of the structure. As shown in section 3 (Figure 3.1) the group velocity in a homogeneous plasma depends on the frequency of light and density of the plasma. Table 5.1 shows the group velocity in a homogeneous plasma of density $n_0 = 0.3n_\mathrm{c}$ (denoted $v_{\mathrm{g},0}$) compared to that obtained in the structure (denoted $v_{\mathrm{g,PPC}}$) as well as the quotient $v_{\mathrm{g,eff}} = v_{\mathrm{g,PPC}}/v_{\mathrm{g},0}$. The structure is seen to have most effect near the band gap where propagation is still a factor two slower. For frequencies far below the band gap the effective slowdown factor approaches unity while for frequencies above the band gap the approach is slower.

It is also of interest to consider the transmission of each pulse. As Figure 5.16 shows, the transmission decreases almost in parallel to the decrease in group velocity. For example at $\omega = 1.08\omega_0$ the transmission was just 40%, furthermore pulses even closer to the band gap were subject to considerable dispersion as a result of the rapid change in group velocity.

Table 5.1: Table of group velocities for different frequencies around the first band gap. The row $v_{\mathrm{g},0}$ shows theoretical group velocities in a homogeneous plasma of density $n_\mathrm{e} = 0.3n_\mathrm{c}$, the row $v_{\mathrm{g,PPC}}$ shows the group velocities obtained in PIC simulation (also Figure 5.15), the row $v_{\mathrm{g,eff}}$ shows the effective group velocity of the structure when accounting for the reduction from the average plasma density.

ω/ω_0	0.84	0.86	0.88	0.90	0.92	1.08	1.10	1.12	1.14	1.16
$v_{\mathrm{g},0}$	0.76	0.77	0.78	0.79	0.80	0.86	0.87	0.87	0.88	0.88
$v_{\mathrm{g,PPC}}$	0.70	0.67	0.62	0.56	0.46	0.43	0.58	0.64	0.70	0.74
$v_{\mathrm{g,eff}}$	0.93	0.87	0.79	0.70	0.57	0.50	0.67	0.73	0.80	0.84

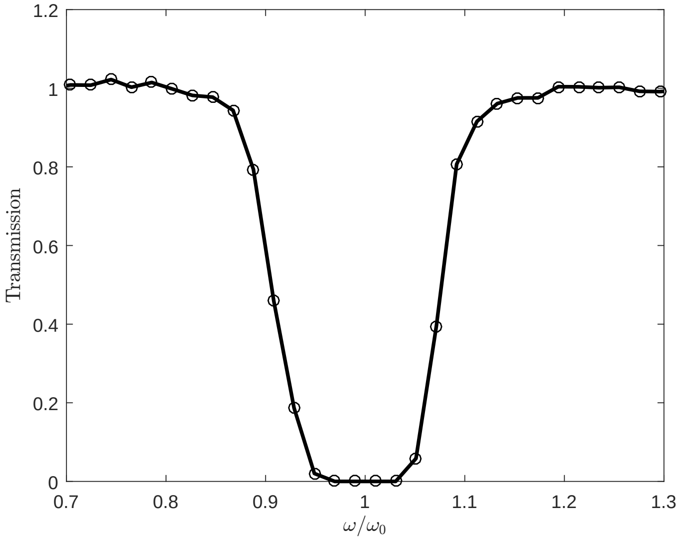

Figure 5.16: Transmission observed in PIC simulations of different frequencies. The structure is the same as that used to find the group velocities in Figure 5.15 and Table 5.1.

For oblique incidence at large enough angles propagation is allowed also for frequencies which lie in the band gap at normal incidence. A grating was formed in a two dimensional simulation from two s-polarised Gaussian pulses as in the one dimensional case. A higher electron temperature was used ($T_e = 50\,\mathrm{eV}$) to increase the Debye length in order to allow the grid spacing to be made larger while still avoiding self heating. To compensate for the smaller grating peak density due to temperature effects a higher driving laser intensity was used of $a_1 = a_2 = 0.06$. The number of particles per cell used was 25. With this the grating develops in a similar manner to the one dimensional case, in particular the calculated band structure at the time when the pulse arrives at the vacuum-plasma boundary is similar to the one in Figure 5.11.

The angles which allow propagation can be read from Figure 5.11 where it is seen that for frequencies of $\omega = \omega_0$ a wavevector of at least $\mathbf{k} = (k_1, 0.35k_0)$ is required which translates to an angle $\theta = \mathrm{atan}\, k_y/k_x = 22.7°$. Figure 5.17 shows the transmission of a 70 fs FWHM Gaussian pulse with peak intensity $I_0 = 1 \cdot 10^{17}\,\mathrm{Wcm}^{-2}$ incident with an angle of $\theta = 28°$, central wavelength $\lambda_0 = 0.8\,\mu\mathrm{m}$ and $8\,\mu\mathrm{m}$ beam diameter.

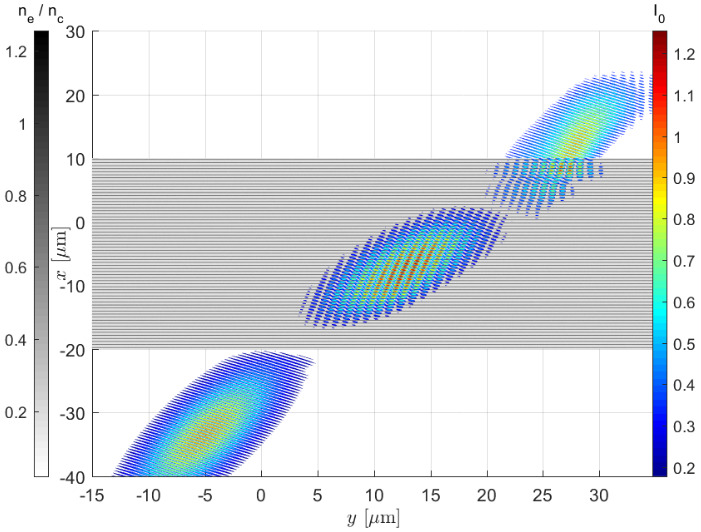

Figure 5.17: Transmission of a 70 fs Gaussian pulse of $8\,\mu\mathrm{m}$ beam diameter (colorscale) and central frequency $\omega = \omega_0$ incident with an angle $\theta = 28°$ on a 2 dimensional density grating similar to that of Figure 5.1 (greyscale). The pulse is shown at three different timesteps, entering from bottom left, with intensity normalised to the maximum intensity $I_0 = 1 \cdot 10^{17}\,\mathrm{Wcm}^{-2}$ of the pulse prior to interacting with the grating. Note that the reflected parts are not shown.

Most of the spectral width of the pulse is outside the band gap, allowing most frequency components to propagate. Reflections do however occur both on the vacuum-plasma boundary and plasma-vacuum boundary which together with the reflections due to the band gap account for total loss of about 10% of the pulse energy.

Some refraction can be observed away from the normal which is expected even in homogeneous plasmas as they have refractive indices $0 \leq n \leq 1$ for $n_\mathrm{e} \leq n_\mathrm{c}$. In simulations of different incidence angle the refraction is observed to be larger than that obtained from the homogeneous plasma with the same average plasma density, for which Snell's law agrees with simulations.

Note that the pulse is compressed slightly inside the grating which increases the intensity to above I_0. The compression can be thought of as occurring due to the front of the pulse starting to move slower while the part of the pulse still outside the grating is moving at c. The increase in maximum intensity is then simply due to conservation of energy. It is of course interesting to note that these TPPCs allow pulses to propagate even though the density exceeds n_c.

Figure 5.18 shows the group velocity of 70 fs FWHM pulses of frequency $\omega = \omega_0$, incident on the same grating as above, as a function of the angle of incidence θ. The group velocity was determined from the velocity of the peak of the pulse envelope. The transmission is also shown in each case. A sharp decline in transmission and group velocity is seen near the theoretical band edge $\theta \approx 22°$. Since the frequency is ω_0 for each case, the effective impact of the structure is obtained by comparing each value of v_g to $v_{\mathrm{g},0}|_{\omega=\omega_0} = 0.836c$. Near the band edge both high reflection and dispersion was observed equivalent to the one dimensional case of varying frequency but here oblique propagation allows the use of the same laser for both driving pulses and probe pulses.

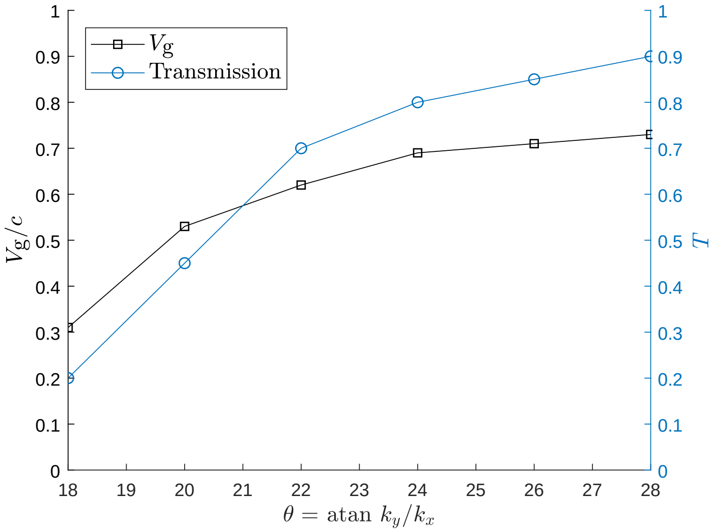

Figure 5.18: Group velocity of 70 fs Gaussian pulse with frequency $\omega = \omega_0$ incident on the grating seen in Figure 5.17 for varying angles (black squares) and the respective transmission of each pulse (blue circles).

Figure 5.19 demonstrates the case of reflection when the angle has been lowered to $\theta = 13°$ where 95% of the incident energy is reflected. The simulation was run with the same parameters as in the case of transmission except with a shorter initial plasma. The reflected pulse can be seen to have a lower maximum intensity as a result of being stretched in the transverse direction. The evanescent wave at the vacuum-plasma boundary can also be seen to decay as it penetrates the outermost periods of the grating, dropping to 10% of the peak initial pulse intensity after five grating periods. The angles allowing reflection and transmission are in good agreement with those of of Lehmann & Spatschek who, however, observed larger peak intensity for the reflected pulse [20].

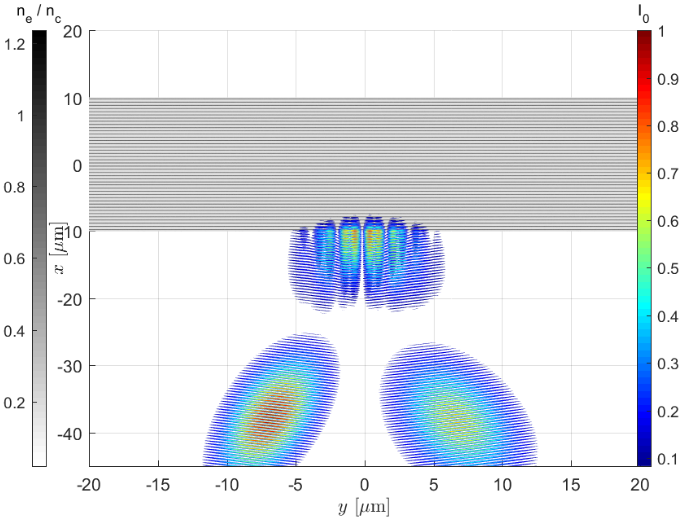

Figure 5.19: Reflection of a 70 fs Gaussian pulse of 8 μm beam diameter (colorscale) and central frequency $\omega = \omega_0$ incident with an angle $\theta = 13°$ on a 2 dimensional density grating similar to that of Figure 5.1 (greyscale). The pulse is shown at three different timesteps, entering from bottom left, with intensity normalised to the maximum intensity $I_0 = 1 \cdot 10^{17}\,\mathrm{Wcm}^{-2}$ of the pulse prior to interacting with the grating. Note that the transmitted parts are not shown.

Almost complete reflections were observed up to intensities of $5 \cdot 10^{17}\,\mathrm{Wcm}^{-2}$ for normal incidence with minor effects on the grating. Initially, when the intensity is increased, only the first two density peaks are affected because this is where the intensity is the highest. The electrons in the peaks are pushed backwards between one and two peak widths by the ponderomotive force, creating thin density spikes of up to several n_c. As the intensity increases beyond $10^{18}\,\mathrm{Wcm}^{-2}$ the pulse penetrates into deeper layers but is still reflected, however it becomes more stretched in the propagation direction. Even higher intensities of $10^{19}\,\mathrm{Wcm}^{-2}$ to $10^{20}\,\mathrm{Wcm}^{-2}$ push through the entire grating, creating a hole in the process. As one would expect, the grating can reflect slightly higher intensities at oblique incidence, compared to normal incidence, as the pulse is spread out on a larger area.

The high reflectance at low angles of incidence together with the wide band gap offers a potential for short pulsed ultra intense slow light without the high loss observed near the band gap. Figure 5.20 demonstrates the idea. Two gratings were placed in parallel with a $2\,\mu\mathrm{m}$ vacuum space in between. In the simulations the gratings were introduced by making a fit to the density grating data with the stationary solution, $f(x) = a + b\mathrm{e}^{-c\cos(2k_1 x)}$, where a, b and c are constants. The other simulation parameters were the same as those used in the simulation of Figure 5.17.

A 70 fs FWHM s-polarised Gaussian pulse with $6\,\mu\mathrm{m}$ diameter enters at an angle of $\theta = 8^\circ$ and is reflected back and forth between the gratings creating a pulse moving in the positive $y-$direction. The initial velocity of the part of the pulse which is coupled into the structure is simply $v = c\sin\theta \approx 0.13c$. A large part of the pulse energy is not coupled and some energy is leaking into the grating on each pass. The pulse is seen to disperse as it propagates and was observed to increase in velocity over time reaching $v = 0.4c$ after propagating $30\,\mu\mathrm{m}$ along the $y-$direction.

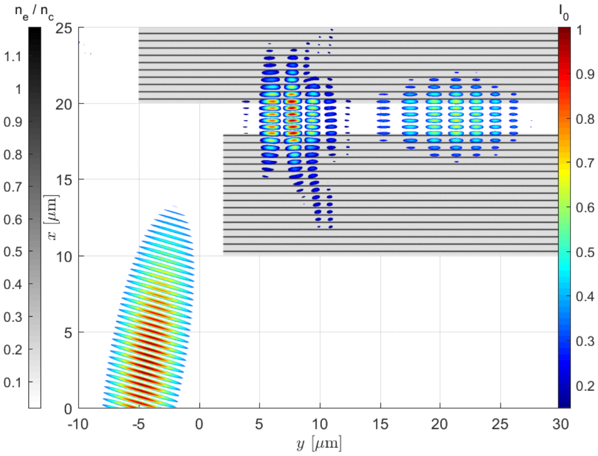

Figure 5.20: Coupling of a 70 fs Gaussian pulse of $6\,\mu\mathrm{m}$ beam diameter (colorscale) and central frequency $\omega = \omega_0$ incident with an angle $\theta = 8^\circ$ on a 2 dimensional density grating similar to that of Figure 5.1 (greyscale). The pulse is shown at three different timesteps, entering from bottom left, with intensity normalised to the maximum intensity $I_0 = 1 \cdot 10^{17}\,\mathrm{Wcm}^{-2}$ of the pulse prior to interacting with the grating.

Chapter 6

Conslusions and Outlook

The aim of this thesis has been to determine the slow light capabilities of 1D transient plasma photonic crystals by PIC code simulations. In addition the goal was to diverge from the ideal simulation parameters in order to investigate some experimental considerations one has to take into account in order to realise the TPPCs using laser systems as that available in the Ultrahigh intensity laser physics group at the division of Atomic Physics, Lund.

Slow light for both normal incidence, using frequencies close to the band gap, and oblique incidence, using the central band gap frequency, have been demonstrated. The results were shown to be in good agreement with the theory of group velocity derived from the slope of dispersion relations obtained using Bloch waves. Pulse velocities of below 50% the speed of light have been observed, consistently below the velocities obtained in an unstructured plasma of the same average density. The transmission was observed to be poor and dispersion high for low pulse velocities.

The observations on the development of the TPPCs from earlier work has been confirmed, furthermore the structures have been shown to converge to a grating of peaks and troughs of uniform amplitudes when allowing the time of overlap of pulses to be neither too long or too short. Additionally, the effect of chirped pulses have been shown to limit the length of TPPCs by invoking a gradual widening of peaks further out from the point where the pulses meet. Also, ions of higher masses have been shown to have a moderate effect on the band gap width, which can be compensated using higher energy driving pulses.

A slow light pulse with initial velocities depending on the angle of incidence has been suggested based on repeated reflections in a wave guide consisting of two PPCs separated by a small space of vacuum. While the coupling efficiency is poor this structure could allow for ultra-high intensity pulses to propagate without the high reflection associated with slow light modes near bandgaps. It would of course have to be confined also in the third dimension as the pulse would otherwise diverge. Furthermore the ponderomotive forces is not as simple as that one used to describe the formation of TPPCs in this thesis as it consists of a semi-standing wave moving transversely. A closer analysis of the nature of the ponderomotive force acting on, possibly relativistic, particles would be necessary to determine whether it could be used to, say, accelerate ions in a two stage process.

Currently, slow light with higher transmission coefficients at low intensities, as used in optical communications, are based on either coupled resonators or line defect waveguides which consist of either holes or pillars of dielectric material in a bulk dielectric slab, with one line of holes/pillars removed. In these cases there is also a direct trade-off between the lowest possible speed and spectral width it permits but wideband slow light have been shown to be possible [10, 11]. Similar structures made entirely out of plasma could possibly offer ultra-intense slow light to propagate with a larger transmission coefficient. For example, using two sets of two counterpropagating driving pulses at a 90° angle produces a two dimensional TPPC which displays large diameter low density circles, or holes, surrounded by high density regions. Due to the dielectric function being smaller in high density plasmas this is most similar to the case of line defect waveguides consisting of high dielectric constant pillars in a vacuum/low dielectric material. Similarly, it could be possible to ionise a material consisting of a grid of near critical density pillars to create the TPPC equivalent to an air hole line defect waveguide.

As a last observation, by sending in a pulse close to the band gap during the down ramp phase of a TPPC, the time dependence of the band gap could be used as a gradual speed up, similar to how the gradual change of density can be used to accelerate a slow relativistic pulse to achieve a gradual ion acceleration as suggested by Brantov et al. [6].

To summarise, more complex TPPCs obtained by counterpropagating (or intersecting) laser pulses could potentially offer slow ultra-intense light over short propagation distances and times but requires further work. In particular further development of reliable near critical density targets is also of importance in order to bridge theory to experiments.

References

[1] V. Yanovsky, V. Chvykov, G. Kalinchenko, P. Rousseau, T. Planchon, T. Matsuoka, A. Maksimchuk, J. Nees, G. Cheriaux, G. Mourou and K. Krushelnick, "Ultra-high intensity- 300-tw laser at 0.1 hz repetition rate.", Optics Express **16**, 2109–2114 (2008).

[2] G. A. Mourou, T. Tajima and S. V. Bulanov, "Optics in the relativistic regime", Reviews of Modern Physics **78**, 309–371 (2006).

[3] S. C. Wilks, A. B. Langdon, T. E. Cowan, M. Roth, M. Singh, S. Hatchett, M. H. Key, D. Pennington, A. MacKinnon and R. A. Snavely, "Energetic proton generation in ultra-intense laser–solid interactions", Physics of Plasmas **8**, 542–549 (2001).

[4] P. Sprangle, G. Joyce, E. Esarey and A. Ting, "Laser wakefield acceleration and relativstic optical guiding", AIP Conference Proceedings **175**, 231–239 (1988).

[5] F. Mackenroth, A. Gonoskov and M. Marklund, "Chirped-standing-wave acceleration of ions with intense lasers", Physical Review Letters **117**, 104801 (2016).

[6] A. V. Brantov, E. A. Govras, V. F. Kovalev and V. Y. Bychenkov, "Synchronized ion acceleration by ultraintense slow light", Physical Review Letters **116**, 085004 (2016).

[7] R. W. Boyd, "Material slow light and structural slow light: similarities and differences for nonlinear optics [Invited]", Journal of the Optical Society of America B **28**, A38–A44 (2011).

[8] L. V. Hau, S. E. Harris, Z. Dutton and C. H. Behroozi, "Light speed reduction to 17 metres per second in an ultracold atomic gas", Nature **397**, 594 (1999).

[9] E. Yablonovitch, T. J. Gmitter and K. M. Leung, "Photonic band structure: the face-centered-cubic case employing nonspherical atoms", Physical Review Letters **67**, 2295–2298 (1991).

[10] C.-Y. Lin, X. Wang, S. Chakravarty, B. S. Lee, W.-C. Lai and R. T. Chen, "Wideband group velocity independent coupling into slow light silicon photonic crystal waveguide", Applied Physics Letters **97**, 183302 (2010).

[11] J. Liang, L.-Y. Ren, M.-J. Yun, X. Han and X.-J. Wang, “Wideband ultraflat slow light with large group index in a w1 photonic crystal waveguide”, Journal of Applied Physics **110**, 063103 (2011).

[12] T. Baba, “Slow light in photonic crystals”, Nature Photonics **2**, Review Article, 465 (2008).

[13] H. Hojo and A. Mase, “Electromagnetic-wave transmittance characteristics in one-dimensional plasma photonic crystals”, Journal of Plasma and Fusion Research **8**, 477 (2009).

[14] H. HOJO and A. MASE, “Dispersion relation of electromagnetic waves in one-dimensional plasma photonic crystals”, Journal of Plasma and Fusion Research **80**, 89–90 (2004).

[15] G. Pandey and S. Ojha, “Band structure, group velocity, effective group index and effective phase index of one dimensional plasma photonic crystal”, Optik - International Journal for Light and Electron Optics **124**, 3514–3519 (2013).

[16] B. Wang and M. A. Cappelli, “A plasma photonic crystal bandgap device”, Applied Physics Letters **108**, 161101 (2016).

[17] S. Suntsov, D. Abdollahpour, D. G. Papazoglou and S. Tzortzakis, “Femtosecond laser induced plasma diffraction gratings in air”, in Conference on lasers and electro-optics/international quantum electronics conference (2009).

[18] A. Leblanc, A. Denoeud, L. Chopineau, G. Mennerat, P. Martin and F. Quéré, “Plasma holograms for ultrahigh-intensity optics”, Nature Physics **13**, 440 (2017).

[19] S. Monchocé, S. Kahaly, A. Leblanc, L. Videau, P. Combis, F. Réau, D. Garzella, P. D’Oliveira, P. Martin and F. Quéré, “Optically controlled solid-density transient plasma gratings”, Physical Review Letters **112**, 145008 (2014).

[20] G. Lehmann and K. H. Spatschek, “Laser-driven plasma photonic crystals for high-power lasers”, Physics of Plasmas **24**, 056701 (2017).

[21] G. Lehmann and K. H. Spatschek, “Transient plasma photonic crystals for high-power lasers”, Physical Review Letters **116**, 225002 (2016).

[22] Z.-M. Sheng, J. Zhang and D. Umstadter, “Plasma density gratings induced by intersecting laser pulses in underdense plasmas”, Applied Physics B **77**, 673–680 (2003).

[23] S. N. Chen, T. Iwawaki, K. Morita, P. Antici, S. D. Baton, F. Filippi, H. Habara, M. Nakatsutsumi, P. Nicolaï, W. Nazarov, C. Rousseaux, M. Starodubstev, K. A. Tanaka and J. Fuchs, “Density and temperature characterization of long-scale length, near-critical density controlled plasma produced from ultra-low density plastic foam”, Scientific Reports **6**, 21495 (2016).

[24] R. Fitzpatrick, *Plasma physics, an introduction* (CRC Press, 6000 Broken Sound Parkway NW, Suite 300 Boca Raton, FL 33487-2742, 2014).

[25] J. Bittencourt, *Fundamentals of plasma physics*, 3rd ed. (Springer-Verlag, 175 Fifth Avenue, New York, NY,10010, 2004).

[26] W. Kruer, *The physics of laser plasma interactions* (Westview Press, 5500 Central Avenue, Boulder, Colorado, 80301-2877, 2003).

[27] F. Chen, *Introduction to plasma physics and controlled fusion*, 1st ed. (Plenum Press, 227 West 17th Street, New York, N.Y. 10011, 1974).

[28] P. W. Smorenburg, J. H. M. Kanters, A. Lassise, G. J. H. Brussaard, L. P. J. Kamp and O. J. Luiten, "Polarization-dependent ponderomotive gradient force in a standing wave", Physical Review A **83**, 063810 (2011).

[29] A. Macchi, *A superintense laser-plasma interaction primer*, 1st ed. (Springer, 2013).

[30] P. Zhang, N. Saleh, S. Chen, Z. Sheng and D. Umstadter, "An optical trap for relativistic plasma", Physics of Plasmas **10**, 2093–2099 (2003).

[31] M. Botton and A. Ron, "Efficiency enhancement of a plasma-filled backward-wave oscillator by self-induced distributed feedback", Physical Review Letters **66**, 2468–2471 (1991).

[32] G. Floquet, "Sur les équations différentielles linéaires à coefficients périodiques", fre, Annales scientifiques de l'École Normale Supérieure **12**, 47–88 (1883).

[33] F. Bloch, "Über die quantenmechanik der elektronen in kristallgittern", Zeitschrift für Physik **52**, 555–600 (1929).

[34] I. Abramowitz M. & Stegun, *Handbook of mathematical functions with formulas, graphs, and mathematical tables*, 9th ed. (Dover Publications, New York, NY, 1970).

[35] C. Kittel, *Introduction to solid state physics*, 8th ed. (John Wiley & Sons, 111 River Street, Hoboken, NJ 07030, 2005).

[36] D. Snoke, *Solid state physics, essential concepts* (Addison-Wesley, 2009).

[37] J. Jackson, *Classical electrodynamics*, 3rd ed. (John Wiley & Sons, 111 River Street, Hoboken, NJ 07030, 2014).

[38] L. Brillouin, *Wave propagation and group velocity* (Academic Press, New York, NY, 1960).

[39] E. Feigenbaum, N. Kaminski and M. Orenstein, "Negative dispersion: a backward wave or fast light? nanoplasmonic examples", Optics Express **17**, 18934–18939 (2009).

[40] A. Figotin and I. Vitebskiy, "Slow wave phenomena in photonic crystals", Laser & Photonics Reviews **5**, 201–213 (2011).

[41] T. D. Arber, K. Bennett, C. S. Brady, A. Lawrence-Douglas, M. G. Ramsay, N. J. Sircombe, P. Gillies, R. G. Evans, H. Schmitz, A. R. Bell and C. P. Ridgers, "Contemporary particle-in-cell approach to laser-plasma modelling", Plasma Physics and Controlled Fusion **57**, 113001 (2015).

[42] K. S. Yee, "Numerical solution of initial boundary value problems involving maxwell's equations in isotropic media", IEEE Transactions on Antennas and Propagation, 302–307 (1966).

[43] A. Taflove, "Application of the finite-difference time-domain method to sinusoidal steady-state electromagnetic-penetration problems", IEEE Transactions on Electromagnetic Compatibility **EMC-22**, 191–202 (1980).

[44] C. K. Birdsall, "Particle-in-cell charged-particle simulations, plus monte carlo collisions with neutral atoms, pic-mcc", IEEE Transactions on Plasma Science **19**, 65–85 (1991).

[45] A. Taflove, *Computational electrodynamics: the finite-difference time-domain method* (Artech House, 685 Canton Street, Norwood, MA 02062, 1995).

[46] A. Birdsall C.K. & Langdon, *Plasma physics via computer simulation* (CRC Press, 175 Fifth Avenue, New York, NY,10010, 2004).

[47] Z. M. Sheng, J. Meyer-ter-Vehn and A. Pukhov, "Analytic and numerical study of magnetic fields in the plasma wake of an intense laser pulse", Physics of Plasmas **5**, 3764–3773 (1998).

[48] P. Sprangle, E. Esarey, J. Krall and G. Joyce, "Propagation and guiding of intense laser pulses in plasmas", Physical Review Letters **69**, 2200–2203 (1992).

Appendix A

Simplified Equations of Motion

Here the simplified cold plasma equations of motion used to describe the laser-plasma interaction in section 2.6 are derived starting from the usual form of the equation of motion of a cold electron fluid

$$\frac{\mathrm{D}\mathbf{P}}{\mathrm{D}t} = \frac{\partial \mathbf{P}}{\partial t} + \mathbf{v}\cdot\nabla\mathbf{P} = -e\left(\mathbf{E} + \frac{1}{c}\mathbf{v}\times\mathbf{B}\right), \tag{A.1}$$

where $\mathrm{D}/\,\mathrm{D}t$ is the full derivative, $\mathbf{P} = \gamma m\mathbf{v}$ is the relativistic momentum and $\gamma = \sqrt{1 + (\mathbf{P}/mc)^2} = \sqrt{1 - (\mathbf{v}/c)^2}$ is the Lorentz factor, also called relativistic factor. The magnetic vector potential $\mathbf{A}(\mathbf{r}, t)$ and electric potential $\Phi(\mathbf{r}, t)$ are given by the relations

$$\mathbf{E} = -\nabla\Phi - \frac{1}{c}\frac{\partial \mathbf{A}}{\partial t}, \tag{A.2}$$

$$\mathbf{B} = \nabla\times\mathbf{A}. \tag{A.3}$$

Inserting these equations into equation (A.1) and introducing the normalised momentum $\mathbf{p} = \mathbf{P}/mc = \gamma\mathbf{v}/c$ gives

$$\frac{\partial \mathbf{p}}{\partial t} + \mathbf{v}\cdot\nabla\mathbf{p} = -\frac{e}{mc}\left[-\nabla\Phi - \frac{1}{c}\frac{\partial \mathbf{A}}{\partial t} + \frac{1}{c}\mathbf{v}\times\nabla\times\mathbf{A}\right]. \tag{A.4}$$

The second term on the left can be rewritten with a vector identity as

$$\begin{aligned} &\mathbf{v}\cdot\nabla\mathbf{p} = \frac{c}{\gamma}\mathbf{p}\cdot\nabla\mathbf{p} = \frac{c}{\gamma}\left[\mathbf{p}\times(\nabla\times\mathbf{p}) - \frac{1}{2}\nabla\mathbf{p}^2\right] = \\ &\frac{c}{\gamma}\left[\frac{\gamma\mathbf{v}}{c}\times(\nabla\times\mathbf{p}) - \gamma\nabla\gamma\right] = \mathbf{v}\times(\nabla\times\mathbf{p}) - c\nabla\gamma. \end{aligned} \tag{A.5}$$

Inserting this into equation (A.4) one finds

$$\begin{aligned}\frac{\partial \mathbf{p}}{\partial t} = \frac{e}{mc^2}\frac{\partial \mathbf{A}}{\partial t} + \frac{e}{mc}\nabla\Phi - \frac{e}{mc^2}\mathbf{v}\times(\nabla\times\mathbf{A}) + \mathbf{v}\times(\nabla\times\mathbf{p}) - c\nabla\gamma \Rightarrow \\ \frac{1}{c}\frac{\partial(\mathbf{p}-\mathbf{a})}{\partial t} = \nabla(\phi-\gamma) + \frac{\mathbf{v}}{c}\times\left[\nabla\times(\mathbf{p}-\mathbf{a})\right],\end{aligned} \tag{A.6}$$

where the normalised scalar potential $\phi = \frac{e}{mc^2}\Phi$ and the normalised vector potential $\mathbf{a} = \frac{e}{mc^2}\mathbf{A}$ have been introduced and $\mathbf{p}-\mathbf{a}$ is the canonical momentum. The following part is outlined in [47, 48]. Taking the curl of both sides of equation (A.6) yields the relation

$$\frac{\partial}{\partial t}\left[\nabla\times(\mathbf{p}-\mathbf{a})\right] = \nabla\times\left\{\mathbf{v}\times\left[\nabla\times(\mathbf{p}-\mathbf{a})\right]\right\}. \tag{A.7}$$

Assuming the canonical momentum is zero before some time t_0 before the laser pulse arrives means $\nabla\times(\mathbf{p}-\mathbf{a}) = 0$ holds initially. This represents the laser not being turned on prior to some time. If this is true, the relation will hold for all later times as well so that equation (A.6) reduces to

$$\frac{1}{c}\frac{\partial(\mathbf{p}-\mathbf{a})}{\partial t} = \nabla(\phi-\gamma) \tag{A.8}$$

Continuing, the plasma density is assumed underdense (equivalent to $\omega_{\mathrm{pe}} \ll \omega_{\mathrm{L}}$) so that the fields can be split into fast and slow components , $\mathbf{a}_f$ and $\mathbf{a}_s$, where the fast field is varying on the timescales of the laser ω_L^{-1} and the slow field on the timescale of the electron ω_{pe}^{-1}. Averaging over one laser cycle to remove the fast oscillations equation (A.8) becomes

$$\frac{1}{c}\frac{\partial(\mathbf{p}-\mathbf{a})}{\partial t} = \nabla(\phi-\bar{\gamma}), \tag{A.9}$$

where the slowly varying component of the relativistic factor is denoted $\bar{\gamma}$.

Appendix B

Populärvetenskaplig Artikel

B.1 Långsamma ljuspulser med ultrahög intensitet i plasmastrukturer

Långsamma pulser är intressanta för acceleration av till exempel protoner. Protoner som accelereras till höga hastigheter kan i förlängningen användas till mer skonsam behandling av cancer, där en större del av energin dödar cancercellerna istället för friska celler runt om. Det är emellertid mycket svårt att få protoner att färdas i de hastigheter som krävs. Konventionella partikelacceleratorer är ofta enorma ringformade byggnader, som kan vara flera kilometer långa. För att vara tillämpbart i vård behövs en kompakt lösning, något som användning av lasrar skulle kunna erbjuda.

För att förstå hur långsamt ljus kan utnyttjas kan man göra en jämförelse med en surfare. Surfaren måste paddla upp i en hastighet som matchar vågens för att bli upplockad och ta del av vågens energi. På ett liknande sätt behöver en proton komma upp i ljuspulsens hastighet för att accelereras, men att få protoner med hög hastighet var precis det problem som skulle lösas. En tänkbar lösning är därför att istället sakta ner ljuset till protonens hastighet.

För att sänka hastigheten på en ljuspuls kan strukturerade material användas, i det här fallet plasmastrukturer. Ett plasma är en joniserad gas, alltså en gas där elektronerna har frigjorts från sina atomer. Genom att använda två motriktade lasrar inne i ett plasma skapas en stående våg, det vill säga en vågform som inte förflyttar sig i sidled utan bara upp och ner. En stående våg kan man enkelt se genom att till exempel hålla ut ett rep mellan två personer och skaka det upp och ner i precis rätt hastighet. I det här fallet består dock vågen av ljusvågor.

Den stående vågen används för att skapa strukturen i plasmat. Förenklat kan man tänka sig att partiklar som befinner sig på toppen av vågen kommer att rulla ner till botten, se Figur B.1. På så vis skapas en upprepande struktur i plasmat med skikt av låg respektive hög densitet. När den stående vågen försvinner återgår plasmat långsamt till att vara jämnt fördelat.

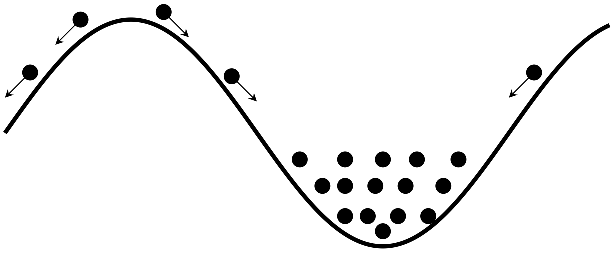

Figur B.1: Plasmastrukturen skapas av den stående vågen.

Så hur kan plasmastrukturen användas för att få långsamt ljus? Man kan tänka sig varje skikt likt en vägg med många små hål. Varje foton (ljuspartikel) har en viss chans att åka igenom och en viss chans att studsa tillbaka. Om en grupp med många fotoner infaller på kort tid (en ljuspuls) studsar de enskilda fotonerna fram och tillbaka mellan skikten ett antal gånger. På så vis tar det i genomsnitt längre tid för den enskilda fotonen att färdas genom strukturen och därmed har även ljuspulsen som helhet färdats långsammare. Figur B.2 illustrerar detta.

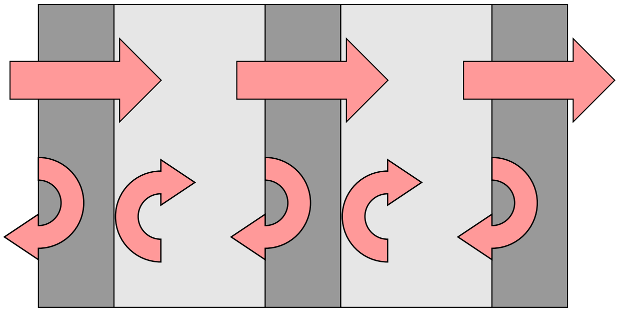

Figur B.2: Schematisk bild av långsamt ljus i strukturer.

Att skikten är uppbyggda av just plasma tillåter ljuspulser med ultrahög intensitet att saktas ner. De höga intensiteterna skulle förstöra vanliga material på ett ögonblick, men är nödvändig för att göra uppställningen kompakt och accelerera protonerna till höga hastigheter på en kort sträcka.

I arbetet undersöks, med hjälp av datorsimuleringar, hur plasmastrukturer kan skapas med stående vågor samt möjligheterna för dessa strukturer att sakta ner ljuspulser med ultrahög intensitet. Simuleringarna visar att ljuspulserna kan saktas in till lägre än halva ljusets hastighet i vakuum. För att accelerera protoner krävs dock hastigheter på närmare 10% av ljusets hastighet. Dessa hastigheter kan uppnås, men de enkla strukturerna har en begränsning: ju långsammare ljuset går desto mindre av ljuset släpps igenom. Det går dock att komma runt den här begränsningen. Genom att använda två jämsides placerade plasmastrukturer, som i Figur B.3, separerade med en smal kanal av vakuum, kan en ljuspuls med hög intensitet studsa fram och tillbaka inne i kanalen och långsamt röra sig framåt längs kanalen. I simuleringar uppnås på så vis pulser med hög intensitet och hastigheter nära 10% av ljusets hastighet i vakuum, där hastigheten längs kanalen beror av vinkeln som ljuspulsen faller in med.

Möjligheten finns även att mer avancerade strukturer skulle kunna ge låga hastigheter som bevarar den höga ljusintensiteten som krävs för protonacceleration. Sådana strukturer kan uppnås genom att till exempel använda fler än två lasrar, riktade mot plasmat i olika vinklar, för att skapa komplicerade stående vågor.

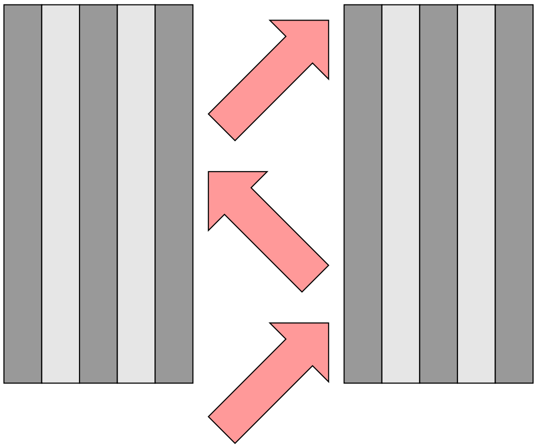

Figur B.3: Schematisk bild av långsamt ljus längs en kanal av vakuum mellan två plasmastrukturer, som i detta fall optimerats för maximal reflektion av intensiva ljuspulser.